Radar characterization of ice crystal orientation fabric and anisotropic rheology within an Antarctic ice stream

Thomas Jordan[1], Carlos Martin[2], Alex Brisbourne[2], Dustin Schroeder[3], and Andrew Smith[2]

[1]University of Bristol
[2]British Antarctic Survey
[3]Stanford

November 21, 2022

Abstract

We use polarimetric radar sounding to investigate variation in ice crystal orientation fabric within the near-surface (top 40-300 m) of Rutford Ice Stream, West Antarctica. To assess the influence of the fabric on ice flow, we use an analytical model to derive anisotropic enhancements of the flow law from the fabric measurements. In the shallowest ice (40-100 m) the azimuthal fabric orientation is consistent with flow-induced development and correlates with the surface strain field. Notably, toward the ice-stream margins, both the horizontal compression angle and fabric orientation tend toward 45 degrees relative to ice flow. This result is consistent with theoretical predictions of flow-induced fabric under simple shear, but to our knowledge has never been observed. The fabric orientation in deeper ice (100-300 m) is significantly misaligned with shallower ice in some locations, and therefore inconsistent with the local surface strain field. This result represents a new challenge for ice flow models which typically infer basal properties from the surface conditions assuming simplified vertical variation of ice flow. Our technique retrieves azimuthal variations in fabric but is insensitive to vertical variation, and we therefore constrain the fabric and rheology within two end-members: a vertical girdle or a horizontal pole. Our hypotheses are that fabric near the center of the ice-stream tends to a vertical girdle that enhances horizontal compression, and near the ice-stream margins tends to a horizontal pole that enhances lateral shear.

Radar characterization of ice crystal orientation fabric and anisotropic rheology within an Antarctic ice stream

T. M. Jordan [1,2,3], C. Martin [4], A. M. Brisbourne [4], D. M. Schroeder [2,5], and A. M. Smith [4]

[1]School of Geographical Sciences, University of Bristol, Bristol, UK.

[2]Department of Geophysics, Stanford University, Stanford, USA.

[3]Plymouth Marine Laboratory, Plymouth, UK.

[4]British Antarctic Survey, Cambridge, UK.

[5]Department of Electrical Engineering, Stanford University, Stanford, USA.

Key Points:

- Variability of ice crystal orientation fabric is inferred from radar in the near-surface of Rutford Ice Stream.
- In the shallowest ice the fabric is consistent with local surface strain whereas in deeper ice this is not always the case.
- The fabric can result in enhancement of horizontal compression in the ice-stream center and lateral shear in the margins.

Corresponding author: Tom Jordan, `tjor@pml.ac.uk`

Corresponding author: Carlos Martin, `cama@bas.ac.uk`

Abstract

We use polarimetric radar sounding to investigate variation in ice crystal orientation fabric within the near-surface (top 40-300 m) of Rutford Ice Stream, West Antarctica. To assess the influence of the fabric on ice flow, we use an analytical model to derive anisotropic enhancements of the flow law from the fabric measurements. In the shallowest ice (40-100 m) the azimuthal fabric orientation is consistent with flow-induced development and correlates with the surface strain field. Notably, toward the ice-stream margins, both the horizontal compression angle and fabric orientation tend toward 45 degrees relative to ice flow. This result is consistent with theoretical predictions of flow-induced fabric under simple shear, but to our knowledge has never been observed. The fabric orientation in deeper ice (100-300 m) is significantly misaligned with shallower ice in some locations, and therefore inconsistent with the local surface strain field. This result represents a new challenge for ice flow models which typically infer basal properties from the surface conditions assuming simplified vertical variation of ice flow. Our technique retrieves azimuthal variations in fabric but is insensitive to vertical variation, and we therefore constrain the fabric and rheology within two end-members: a vertical girdle or a horizontal pole. Our hypotheses are that fabric near the center of the ice-stream tends to a vertical girdle that enhances horizontal compression, and near the ice-stream margins tends to a horizontal pole that enhances lateral shear.

Plain Language Summary

The softness of glacier ice is dependent on the direction which ice crystals are pointing relative to an applied load. This 'ice crystal orientation fabric' also contains information about past ice flow. Compared with the interior of ice sheets, the relationship between fabric and ice flow is relatively unexplored in the ice streams and outlet glaciers which drain the Antarctic Ice Sheet. We use a ground-based geophysical method to investigate how ice fabric varies spatially within Rutford Ice Stream, West Antarctica. We then input the measurements into an ice-flow model to calculate the relative softness of ice for deformation in different directions. Our results reveal rapidly varying fabric orientation within the flow unit. In the shallowest ice, the fabric is consistent with what would be expected from the surface deformation, whereas in deeper ice this is not always true. We then show that the fabric is likely to make the ice softer to horizontal compression in the center of the ice stream and lateral shear in the margins.

1 Introduction

The flow of glacier ice is controlled by its rheology which determines how ice deforms under an applied stress. A range of factors influence the rheology of ice including temperature, microstructural properties such as ice crystal orientation fabric and grain size, damage to the ice, and the character of the underlying stress regime (Cuffey & Paterson, 2010). Ice crystal orientation fabric, from herein referred to as 'fabric', describes the distribution of the orientation of individual crystals. Ice crystallizes in layers, often referred to as basal planes, which have their orientation referenced by a normal vector known as the crystallographic axis (c-axis). The ice fabric is the primary control on anisotropic rheology (i.e. when ice is softer or harder for different stress components). In addition to influencing present-day deformation, ice fabric encodes strain history due to there being a rotation of the c-axes toward the compressive strain axis (direction of least-extension) (Azuma & Higashi, 1985; Alley, 1988; Wang et al., 2002).

To model the influence of fabric on ice flow a range of anisotropic flow-laws for polycrystalline ice have been developed. These flow-laws incorporate either a tensorial relationship for bulk ice viscosity (or its inverse, fluidity) based on the fabric microstructure (Azuma & Goto-Azuma, 1996; Godert, 2003; Gillet-chaulet et al., 2005; Gagliardini et al., 2009; Budd et al., 2013; Faria et al., 2014) or an empirical parameterization based on the stress field (Budd et al., 2013; Graham et al., 2018). In both formulations, anisotropic flow-laws demonstrate that fabric can have a pronounced effect on large-scale ice-sheet flow (Ma et al., 2010; Graham et al., 2018). However, primarily due to the scarcity of measurements, it is often unclear how ice fabric, and its spatial variability impact on ice flow and stability across the ice sheets.

The effects of ice fabric and anisotropic rheology on ice-sheet flow are best characterized at slow-flowing divides and domes where there are often direct fabric measurements available from ice cores (e.g. Montagnat et al. (2014); Kluskiewicz et al. (2017)). At ice domes, deformation is dominated by vertical compression which induces a fabric where the c-axes cluster in the vertical direction, which is often referred to as a vertical pole or single maximum fabric. A vertical pole fabric results in anisotropic ice being softer to horizontal shearing (vertical gradients in horizontal velocity) and harder to vertical compression than isotropic ice (Azuma & Goto-Azuma, 1996; Thorsteinsson

et al., 1997), the latter property impacting on the age-depth relationship (Pettit et al., 2007; Martin et al., 2009). As horizontal shearing dominates the deformation of grounded ice, pole-like fabrics are predicted to result in significant enhancement of ice flow across an ice sheet (Ma et al., 2010). At ice divides, where there is horizontal extension present, vertical girdle fabrics (*c*-axes orientated in a plane perpendicular to the extension direction) develop at moderate ice-depths (Wang et al., 2002; Montagnat et al., 2014; Kluskiewicz et al., 2017). Vertical girdle fabrics are predicted to soften and harden ice to uniaxial strain (compression and extension) in different directions (van der Veen & Whillans, 1994; Ma et al., 2010).

In fast-flowing ice streams there are fewer direct measurements of ice fabric available and geophysical techniques, including passive seismics (E. C. Smith et al., 2017), active seismics (Picotti et al., 2015), radar sounding (Jordan, Schroeder, et al., 2020), provide an alternative means to measure fabric. Taken together, ice stream fabric measurements demonstrate distinct variability, with single-pole, multiple-pole, vertical girdle, and random fabrics all present in different geophysical surveys (Jackson & Kamb, 1997; Horgan et al., 2011; Picotti et al., 2015; E. C. Smith et al., 2017; Jordan, Schroeder, et al., 2020). We typically expect lateral shear (horizontal gradients in horizontal velocity) to dominate the near-surface deformation at ice stream margins, with along-flow extension becoming important in the center of the ice stream. However, this picture is an oversimplification and ice streams also exhibit 'ice-flow complexity' with alternating bands of flow-convergence and divergence (Ng, 2015) and along-flow compression (Minchew et al., 2016) often present. In correspondence with variable deformation behavior, anisotropic rheology is also anticipated to vary within ice streams. For example, Minchew et al. (2018) inferred that ice fabric has a softening effect on lateral shear within the margins of Rutford Ice Stream. Additionally, within the same ice stream, E. C. Smith et al. (2017) showed that a combination of vertical and horizontal c-axis alignment leads to enhanced horizontal shearing in a vertical plane aligned with the ice flow direction.

Here we build upon the previous characterization of ice fabric and its impact on rheology within Rutford Ice Stream using polarimetric radar sounding. This technique is sensitive to crystallographic preferred orientation in the horizontal plane, perpendicular to the radar propagation direction, that we will refer to as 'azimuthal fabric anisotropy'. Specifically, we characterize how crystal fabric orientation varies spa-

tially within the near-surface of the ice stream (top 300 m) and compare with the ice-surface strain field. The fabric estimation uses a recently-developed polarimetric coherence (phase-based) method (Dall, 2010; Jordan et al., 2019; Jordan, Schroeder, et al., 2020). This method exploits analogous principles to radar interferometry, using the polarimetric coherence to place precise constraints on the azimuthal fabric orientation and azimuthal strength. Radar fabric estimates have typically been used to investigate ice-flow history (Fujita et al., 2006; K. Matsuoka et al., 2012; Brisbourne et al., 2019), but have not been used to constrain anisotropic rheology. To address this deficiency we develop a new framework where radar fabric measurements are used to parameterize an anisotropic flow-law (Godert, 2003; Gillet-chaulet et al., 2005; Martin et al., 2009).

This paper is organized as follows. In Section 2 we describe the survey region, data acquisition, and computation of the ice-surface strain field. In Section 3 we outline a representation of ice fabric that is specific to the azimuthal anisotropy that can be measured with radar sounding. In Section 4 we present the polarimetric coherence method used to estimate the fabric, detailing ongoing improvements to the technique. In Section 5 we develop a scheme to parameterize an anisotropic flow law and hence constrain anisotropic rheology. In Section 6 we present results for spatial development in ice fabric and associated anisotropic rheology within the Rutford Ice Stream. In Section 7 we discuss the implications of the study, with a focus on fabric development and fabric enhancement of deformation within ice streams.

2 Survey region, data acquisition, and calculating ice-surface strain

2.1 Survey region

Rutford Ice Stream, West Antarctica, flows approximately southwards into the Filchner-Ronne Ice Shelf and is bounded the Fletcher Promontory and Ellsworth Mountains to the east and west respectively, Figure 1a. The survey region, Figures 1b and 1c, is located approximately 40-80 km upstream of the grounding line where the ice stream is approximately 25 km wide, with ice-flow speed approximately 340 m a^{-1} (Rignot et al., 2011, 2017). The ice thickness within the survey region is approximately 2.2 km (King et al., 2016).

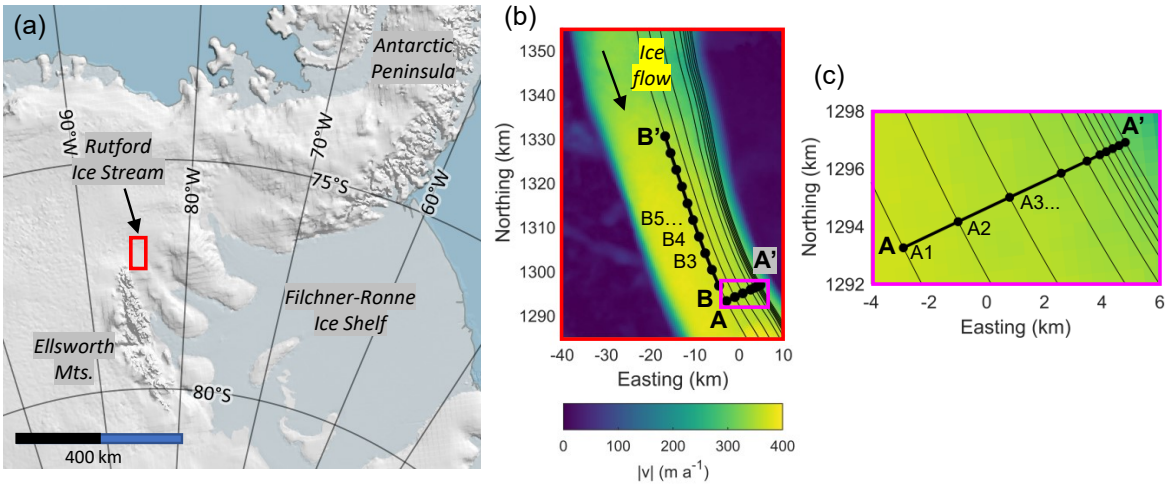

Figure 1. Glaciological setting and radar measurement sites. (a) Location of Rutford Ice Stream and survey region (red box). (b) Survey transects (thick black lines), measurement sites (black circles), and ice-flow streamlines (thin black lines) underlain by ice surface speed, $|v|$. (c) Zoom to Transect A (indicated by pink box in (b)). The maps in (b) and (c) were generated using Antarctic Mapping Tools (Greene et al., 2017) and assume a reference meridian 83.8°W.

The ground-based radar survey consists of two separate transects. Transect A, collected on January 20th 2017, is orientated perpendicular to the ice flow direction. It consists of 10 sites (labeled A1-A10 from west to east) between the center streamline and the ice-stream margin and is of total length 8.5 km with the inter-site spacing decreasing toward the ice-stream margin. Transect B, collected on December 5th 2019, is orientated parallel to the central flowline. It consists of 10 sites (labeled B1-B10 from south to north) with the first site 4 km upstream of site A1 and the inter-site distance spacing fixed at 4 km.

2.2 Polarimetric data acquisition

At each survey site, polarimetric radar-sounding measurements were made using an autonomous phase-sensitive radio-echo sounder (ApRES), a frequency-modulated continuous-wave radar. The ApRES has a center frequency of 300 MHz and a bandwidth of 200 MHz which results in an in-ice range resolution of approximately 40 cm. Further radar system details are provided by Brennan et al. (2014) and Nicholls et al. (2015).

The material anisotropy in the horizontal plane, perpendicular to vertical propagation of the radar is determined from the differences in the returns from four sets of transmit and receive antenna orientations. These are referred to as 'quad-polarized' acquisitions and are obtained by sequentially rotating the transmit and receive antennas (horizontally separated by $\approx$ 8 m) by 90°. We notate the quad-polarized measurements in an HV basis, where H and V notate that the polarization plane is parallel to true west/east and north/south respectively. The data were recorded with respect to magnetic north and subsequently corrected to geographic coordinates by applying a declination of 40°E (assumed constant for the survey).

To range process the raw data we follow Brennan et al. (2014) and obtain a set of four complex amplitudes s_{HH}, s_{VH}, s_{HV}, s_{VH}, where the first and second subscripts indicates the transmit and receive polarization states respectively. The complex amplitudes constitute the scattering matrix, $S_{HV} = [s_{HH}, s_{HV}; s_{VH}, s_{VV}]$, which relates the phase and magnitude of the transmitted and received electric field for each polarization state (Boerner, 1992; Doake et al., 2003).

2.3 Calculating the ice-surface strain field

Of interest in this study is the relationship between the horizontal part of the ice-surface strain-rate tensor, $\mathbf{D}$, and the fabric and rheology estimates (also formulated as the horizontal part of their respective tensors). In the data analysis we express $\mathbf{D}$ in the principal coordinate system (the maximum and minimum strain axes, x_{max} and x_{min}) and a local ice-flow coordinate system (x axis parallel and y axis perpendicular to ice flow). The principal coordinates are appropriate to understand fabric development, and the ice-flow coordinates are appropriate to understand the effects of anisotropic rheology on ice deformation.

$\mathbf{D}$ was initially computed in polarstereographic coordinates by differentiating horizontal ice-surface velocity components from the MEaSUREs data product (Rignot et al., 2011, 2017) which is supplied at an approximately 440 m grid resolution. The velocity derivative procedure follows Jordan, Schroeder, et al. (2020), and uses a convolution derivative with Gaussian kernel and standard deviation $\approx$ 1.8 km. The principal strain rates, D_{max} and D_{min}, corresponding to the strain along x_{max} and x_{min}, were then obtained by solving the eigenvalue problem. The strain rates in the ice-stream

coordinates, D_{xx} (uniaxial strain along-flow), D_{yy} (uniaxial strain across-flow) and D_{xy} (lateral shear in the ice-flow coordinates) were obtained via an azimuthal rotation transform of $\mathbf{D}$.

The strain-rate uncertainty was estimated via propagation of the standard error on the velocity components (Rignot et al., 2011, 2017). This was done numerically by generating an ensemble of velocities uniformly distributed within their provided uncertainty, and then computing spatial velocity derivatives. The strain rate estimates and their uncertainty were then derived from the mean and standard deviation of the velocity derivative ensemble.

3 Representation of ice crystal orientation fabric

3.1 The second-order orientation tensor

Following previous polarimetric radar-sounding studies (Fujita et al., 2006; K. Matsuoka et al., 2012; Brisbourne et al., 2019; Jordan et al., 2019; Jordan, Schroeder, et al., 2020), we model the ice crystal orientation fabric (c-axis orientation distribution) using the second-order orientation tensor, $\mathbf{a}$ (Woodcock, 1977). The tensor eigenvalues, a_1, a_2, a_3 represent the relative c-axis concentration along each principal coordinate direction x_1, x_2, x_3 (from herein referred to as 'fabric eigenvalues' and 'fabric eigenvectors'). The fabric eigenvalues have the properties $a_1 + a_2 + a_3 = 1$, and $a_3 > a_2 > a_1$. The principal coordinates correspond to a base system where the orientation tensor is diagonal and therefore easier to interpret. The principal coordinates are generally not aligned with ice flow.

The second-order orientation tensor is a simplified representation of the fabric that, in general, can be represented as an expansion of even-order orientation tensors (Gillet-chaulet et al., 2005). Only the second-order tensor can be measured using radar methods, which means that higher-order features (e.g. multiple poles) cannot be discriminated. Under the second order tensor representation, ice fabrics can be categorized using the following end-members: 'random/isotropic' ($a_1 \approx a_2 \approx a_3 \approx \frac{1}{3}$), 'single-pole' ($a_1 \approx a_2 \approx 0, a_3 \approx 1$) and 'girdle' ($a_1 \approx 0, a_2 \approx a_3 \approx \frac{1}{2}$).

In this study we decompose the strength of the ice crystal orientation fabric into two degrees of freedom: the girdle strength $G = 2(a_2 - a_1)$ and the pole strength $P = (a_3 - a_2)$, which both range from zero to unity (Kluskiewicz et al., 2017). The fabric

strength is used instead of the eigenvalues, as the radar method measures eigenvalue differences rather than absolute values.

3.2 Assumptions about the fabric orientation in polarimetric radar sounding

In downward-looking radar sounding, the radio wave polarizations are parallel to the ice surface. Consequently, as the radio polarizations are sensitive to material properties in the direction which they oscillate, the technique detects fabric anisotropy, at a given depth, in a horizontal plane parallel to the ice surface. From herein, we will refer to this as 'azimuthal fabric anisotropy'. Previous radar-sounding studies have all assumed that the x_3 axis (direction of greatest c-axis alignment) is vertical, with the x_1 and x_2 axes in the horizontal (e.g. Fujita et al. (2006); K. Matsuoka et al. (2012); Brisbourne et al. (2019); Jordan et al. (2019). This assumption is valid in slow-flow regions such as ice divides and domes, where vertical compression is the dominant stress component. Under this assumption, the radar enables characterization of the 'vertical girdle' aspects of the fabric: the orientation of the x_1 and x_2 eigenvectors and girdle strength, G=2($a_2 - a_1$). In parts of fast-flowing ice-streams, where horizontal stresses are dominant, seismic fabric measurements are consistent with the x_3 and x_2 axes being horizontal and the x_1 axis vertical (E. C. Smith et al., 2017). Under this assumption, the radar enables characterization of the 'horizontal pole' aspects of the fabric: the orientation of the x_3 and x_2 eigenvectors and pole strength, P=($a_3 - a_2$). Modelling radio propagation where one of the fabric eigenvectors is not aligned with the vertical is considerably more complex (K. Matsuoka et al., 2009; Jordan, Besson, et al., 2020), and is further unconstrained from downward-looking radar sounding.

In this study, we consider both vertical girdles (x_3 vertical) and horizontal poles (x_1 vertical) as sources of azimuthal fabric anisotropy. In general, these descriptions refer to 'non-ideal' fabrics where G and P can be significantly less than 1. The orientation of the vertical girdle is quantified using θ_G (the azimuthal angle of the x_2 axis assuming x_3 is vertical) and the orientation of the horizontal pole is quantified using θ_P (the azimuthal angle of the x_3 axis assuming x_1 is vertical). For simplicity, in the polarimetric methods (Section 4), we make the default assumption that we are measuring a vertical girdle, and refer to θ_G and G as the measured degrees of freedom.

3.3 Representing the girdle-pole space

We now consider how a measurement of either G or P (under the assumption either x_3 or x_1 is vertical) constrains the set of three eigenvalues, a_3, a_2, a_1. Due to the additional constraint $a_3 + a_2 + a_1$=1, a pair of G and P values uniquely define a_1, a_2, a_3. The dependence of a_1, a_2 and a_3 on G and P is shown in Figure 2. The upper left corner (G=0, P=1) is a single pole fabric, the lower left corner is a random fabric (G=0, P=0) and the lower right corner is a vertical girdle fabric (G=1, P=0). The 'GP decomposition' is analogous to the 'Woodcock K value decomposition' (Woodcock, 1977) but is formulated for eigenvalue differences rather than log-ratios.

For illustrative purposes, we assume that G is measured by radar and P is unconstrained (x_3 vertical). Due to the triangular shape of the GP space (which arises from the inequality $a_3 > a_2 > a_1$) the range of possible values for P (and therefore a_3, a_2, a_1) is better constrained for higher values of G. This dependency is illustrated by considering minimum and maximum pole bounds, $P_{min} = 0$ and P_{max}, for two radar measurements of differing girdle strengths: G=0.2 and G=0.8 (points **I-IV** in Figure 2a). The respective c-axis distributions are simulated in Figure 2d.

In slow-flow regions, where the vertical girdle assumption holds and G is measured by radar, ice-core fabric data (e.g. Montagnat et al. (2014); Kluskiewicz et al. (2017)) gives a good indication of how P is likely to vary with ice depth. In particular, P generally increases with ice depth, with deeper ice being significantly closer to P_{max} than shallower ice. However, even in relatively shallow ice P is likely to be significantly greater than $P_{min} = 0$. For example, the fabric at the Greenland ice cores corresponds to $P \approx 0.25$ at z $\approx$ 40 m (Montagnat et al., 2014).

4 Polarimetric data analysis

4.1 Overview of method

The procedure to estimate ice fabric from the polarimetric radar data is based on a previously-developed polarimetric coherence method (Dall, 2009, 2010; Jordan et al., 2019; Jordan, Schroeder, et al., 2020). The method exploits the fact that azimuthal fabric anisotropy results in a bulk ice birefringence, a dielectric material property which results in the radio wave phase velocity being a function of polarization. The term 'polarimetric coherence' refers to a phase-correlation method that is

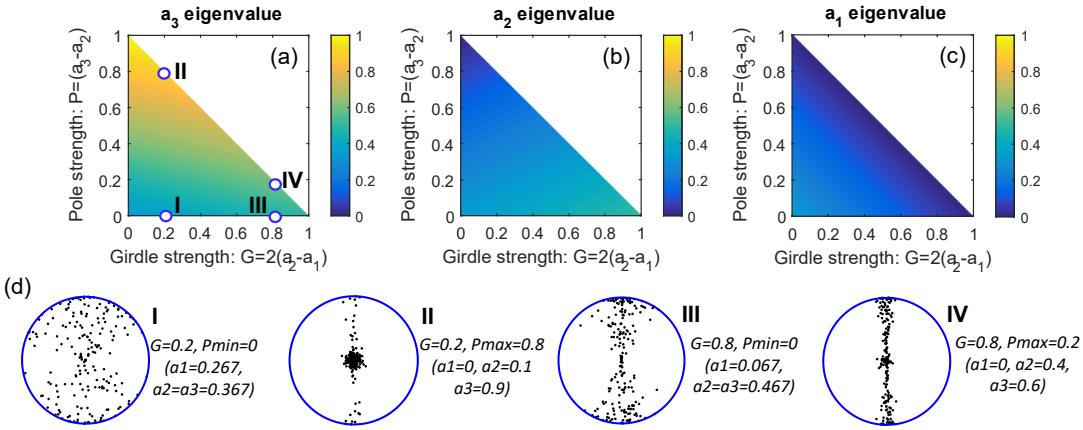

Figure 2. Top row: Fabric eigenvalues as a function of girdle and pole parameters: (a) a_3, (b) a_2, (c) a_1. Bottom row: (d) Examples of synthetic c-axis distributions for four points in GP space, illustrating pole bounds for a measured girdle strength. Points **I** and **II** correspond to the lower (P_{min}) and upper (P_{max}) pole bounds for G=0.2 and points **III** and **IV** corresponds to P_{min} and P_{max} for G=0.8. The c-axis distributions assume an azimuthal equal-area projection where grains in the center of the circle correspond to vertical c-axes and grains on the edge correspond to horizontal c-axes. The sampling procedure used to generate the plots is described by Rongen (2019).

then used to measure the polarimetric phase difference. The measured form of the polarimetric phase difference, the *hhvv* coherence phase (ϕ_{hhvv}), is analogous to the interferometric phase in radar interferometry, but relates to material anisotropy due to the fabric rather than a physical displacement. The polarimetric coherence method reduces ambiguities from using radar power to estimate ice fabric, and better enables measurement uncertainty to be incorporated (Jordan et al., 2019; Jordan, Schroeder, et al., 2020).

In Section 4.2 we outline the key principles in the coherence data analysis. In Section 4.3 we describe new method development that improves automation of the fabric estimates. The coherence method is underpinned by a polarimetric backscatter model of the ice-sheet which relates the ice fabric parameters to the measured scattering matrix and derived quantities (Fujita et al., 2006; Jordan et al., 2019). A reader requiring a full electromagnetic treatment of the backscatter model is referred to Fujita et al. (2006). A reader requiring a presentation of how the coherence methodology relates to the backscatter model is referred to Jordan et al. (2019) with initial proof-of-concept of the technique by Dall (2009, 2010).

4.2 Polarimetric coherence: key principles

The polarimetric coherence analysis is formulated in a 'multi-polarization plane' basis (co-polarized complex amplitude data as a function of azimuthal angle). Following Jordan et al. (2019), the multi-polarization data are notated by h and v where the orientation of h and v is a function of the bearing angle θ, measured in a counter-clockwise direction from true east, Figure 3a. When θ=0° and 180°, h is aligned with H (true east/west) and v is aligned with V (true north/south). To generate the multi-polarization data from the quad-polarized acquisition, a rotation basis transformation was applied to the scattering matrix and validated by checking for conserved quantities (Boerner, 1992). The azimuthal angle of the fabric, for vertical girdle and horizontal pole assumptions, is referenced to the polarizations in Figures 3b and 3c. From herein, we described the measurements in terms of the vertical girdle end-member.

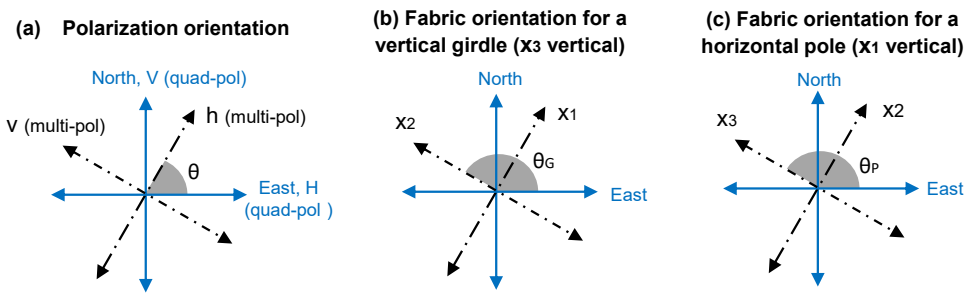

Figure 3. (a) Orientation convention for radar polarization planes in quad- and multi-pol bases. The data analysis is performed in geographical coordinates by applying a prior magnetic declination correction of 40°E. The azimuthal angle, θ, is by convention measured positive in a counter-clockwise direction from true east. (b,c) Orientation convention for fabric eigenvectors assuming the measured fabric is either a non-ideal vertical girdle or a non-ideal horizontal pole.

The polarimetric ($hhvv$) coherence is calculated as a function of azimuthal angle and ice depth by windowing data in the range direction using

$$c_{hhvv}(\theta, z) = \frac{\sum_{j=1}^{N} s_{hh,j} . s_{vv,j}^{*}}{\sqrt{\sum_{j=1}^{N} |s_{hh,j}|^2} \sqrt{\sum_{j=1}^{N} |s_{vv,j}|^2}}, \tag{1}$$

where j is the range bin index and represents a depth, N is the number of independent range pixels, and $*$ indicates complex conjugate. In the data analysis we assume a sliding range window of 40 m, corresponding to N =96 (refer to the Supporting Information, Figures S7 and S8, for sensitivity experiments). c_{hhvv} is a complex number where the magnitude, $|c_{hhvv}|$, describes the correlation between s_{hh} and s_{vv} and ranges from zero to unity. The complex argument

$$\arg(c_{hhvv}) = \phi_{hhvv} = \phi_{hh} - \phi_{vv}, \tag{2}$$

referred to as the $hhvv$ coherence phase, defines the relative polarimetric phase shift between co-polarized acquisitions that are offset by 90° azimuth to each other. The Cramer-Rao bound (Touzi & Lopes, 1999) can be used to estimate the phase error from $|c_{hhvv}|$ via

$$\sigma_{\phi_{hhvv}} \approx \frac{1}{|c_{hhvv}|} \sqrt{\frac{1 - |c_{hhvv}|^2}{2N}}. \tag{3}$$

The central equation which connects ϕ_{hhvv} to the ice fabric is given by

$$\left(\frac{d\phi_{hhvv}}{dz}\right)_{\theta=\theta_G, \theta=\theta_G+90^\circ} = \mp \frac{4\pi f_c}{c} \frac{\Delta\epsilon' G}{\sqrt{\bar{\epsilon}}}, \tag{4}$$

where f_c is the radar center frequency, c is the radio wave speed, $\bar{\epsilon}$ is the mean (polarization averaged) permittivity, $\Delta\epsilon' = (\epsilon_{\|c} - \epsilon_{\perp c})$ is the birefringence of an ice crystal with $\epsilon_{\|c}$ and $\epsilon_{\perp c}$ the permittivity parallel and perpendicular to the c axis. The temperature- and frequency-dependence of the ice permittivity is summarized by Fujita et al. (2000), T. Matsuoka et al. (1996) and Fujita et al. (2006). Here we assume commonly-used values within radar-sounding of $\Delta\epsilon'$=0.034 and $\bar{\epsilon}$=3.15. A negative phase gradient, $\frac{d\phi_{hhvv}}{dz} < 0$, occurs when $\theta = \theta_G$ as the h polarization is aligned with a higher permittivity than the v polarization, and therefore has a lower phase velocity. In turn, the higher permittivity is associated with a greater azimuthal c-axis alignment (the x_2 axis for a vertical girdle). For a measurement of a horizontal pole, G is replaced by $\frac{P}{2}$ in equation (4). In the data analysis, $\frac{d\phi_{hhvv}}{dz}$ was computed using a convolution derivative (analogous to the surface strain derivative in Section 2.3) with the Gaussian kernel standard deviation size matching the coherence bin size.

Following Jordan, Schroeder, et al. (2020), we take into account the effects of phase de-ramping in the ApRES processing (Brennan et al., 2014) by taking the complex conjugate of c_{hhvv}, but do not notate this explicitly in the data analysis.

4.3 Automated extraction of ice fabric

To demonstrate how the fabric estimation is automated we input synthetic data (depth profiles for $\theta_G(z)$ and $G(z)$) into the polarimetric backscatter model (Fujita et al., 2006; Jordan et al., 2019) and compare with the retrieved data-fits. In the fitting, we incorporate two sources of uncertainty. First, we incorporate uncertainty in the antenna/polarization plane alignment by assuming an alignment uncertainty of $\pm$ 5° for each HV acquisition pair. Second, we incorporate uncertainty due to phase decoherence ($|c_{hvvv}|$ <1) by evaluating, equation (3), for measured values of $|c_{hvvv}|$. Further details of how this uncertainty is propagated within the processing chain are given in the Supporting Information (Figure S1).

We illustrate the approach using three examples of increasing complexity. In the synthetic examples, $|c_{hvvv}|$ is modeled using a linearly decreasing ramp function with ice depth, which approximates the decoherence of the ice-stream data in Section 6.2. The first example, Figure 4a, considers depth-invariant girdle orientation and increasing girdle strength with ice depth. The second example, Figure 4b, considers

90° azimuthal rotation within the ice column. The third example, Figure 4c, considers a gradual (non-90°) girdle rotation with ice-depth. Fabric estimation which approximates Case 1 has been validated using ice core fabric data and comparative analysis between different radar systems (Dall, 2010; Li et al., 2018; Jordan et al., 2019).

The data-fitting first solves for $\theta_G(z)$ then $G(z)$. To fit for $\theta_G(z)$ we exploit the fact that $\frac{d\phi_{hhvv}}{dz}$ has either exact, Figures 4a and 4b, or approximate, Figure 4c, azimuthal reflection symmetry about θ_G. To implement the constraint, and solve for $\theta_G(z)$ numerically, we minimized a cost function at each ice depth (see Supporting Information, Section 1). Once $\theta_G(z)$ is established, $G(z)$ is obtained by substituting $(\frac{d\phi_{hhvv}}{dz})_{\theta=\theta_G}$ into equation (4).

The examples in Figure 4(a) and (b) illustrate agreement between the synthetic and fitted values of θ_G. In the deeper ice, the accuracy of the estimates decreases with $|c_{hhvv}|$ due to the related coherence phase error, equation (3). Additionally, at the depth when θ_G rotates by 90° in Figure 4b the estimates for $G(z)$ are impacted by the assumed 40 m window size. The third example illustrates that non-90° rotations can result in biases in the data-fits. The sense of rotation is, however, correctly accounted for. The examples show that the fits for $G(z)$ are generally less robust than θ_G in the presence of phase decoherence. In the data analysis, Section 6.2, we demonstrate that the fabric is well-approximated by the first and second examples, and example 3 is intended to guide method development that may be required in future studies.

The backscatter model simulations in Figure 4 all assume isotropic reflection from the englacial layers. However, due to preserved azimuthal symmetry properties (Jordan et al., 2019), the fitting approach also generalizes to anisotropic reflectors. Isotropic reflection encompasses reflection from conductivity, density, and some classes of fabric reflectors, whereas anisotropic reflection arises purely from fabric reflectors (Fujita et al., 1999).

All the analysis in this section can be interpreted in terms of a horizontal pole fabric with θ_G replaced by θ_P and G replaced by $\frac{P}{2}$.

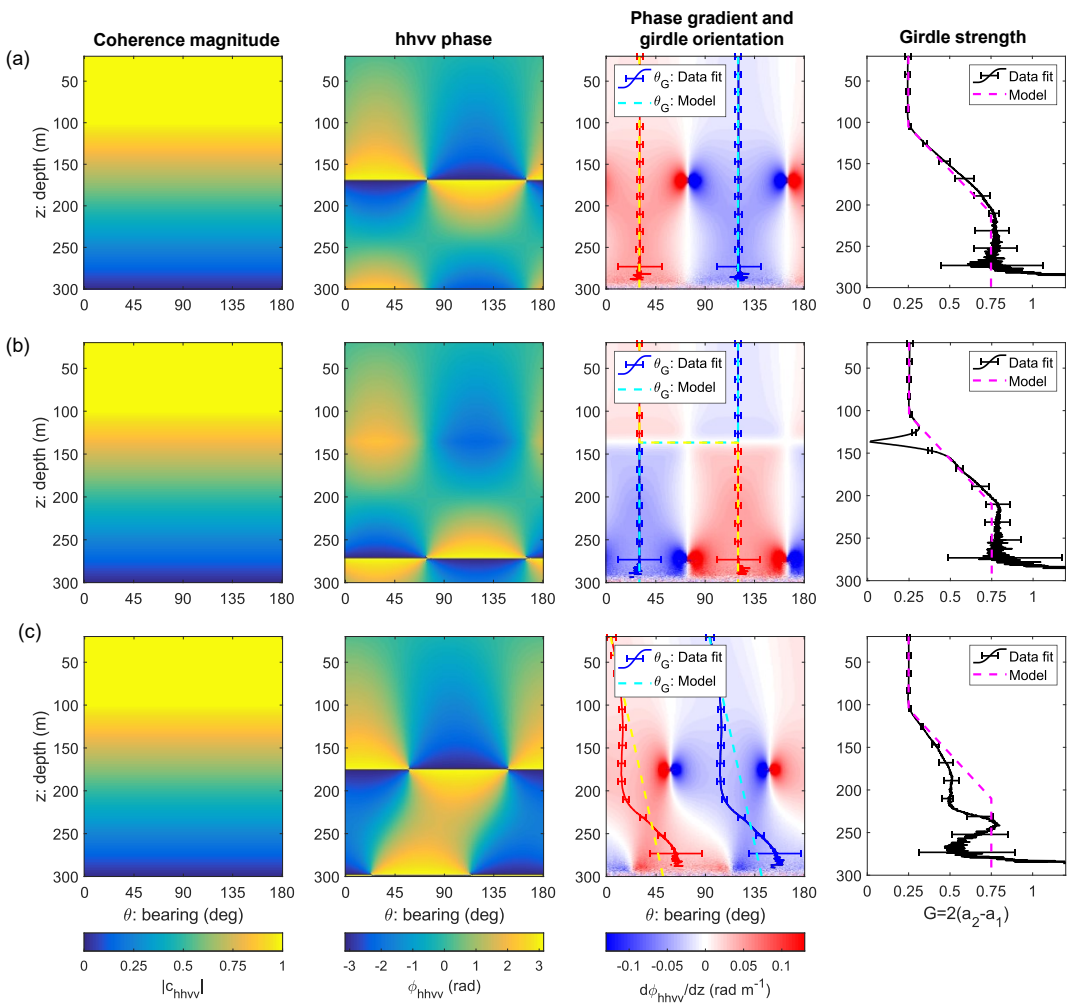

Figure 4. Illustration of fabric estimation using the polarimetric backscatter model with synthetic data. (a) Case 1: Depth-invariant fabric orientation. (b) Case 2: Sharp (90°) azimuthal rotation. (c) Case 3: Gradual azimuthal rotation. In the plot legends 'Model' refers to synthetic fabric data and 'Data-fit' refers to fabric estimates made using an azimuthal reflection symmetry constraint, as applied in the data analysis. θ_G corresponds to the azimuthal angle of the x_2 axis and the model and data-fits for the x_1 axis are indicated by the yellow dashed and solid red lines respectively.

5 Characterization of anisotropic ice rheology

5.1 Overview of anisotropic flow-law and fluidity tensor

The aim of the rheological modeling is to provide a scheme where the radar fabric measurements can be input into an anisotropic flow-law Gagliardini et al. (2009). The flow-law is formulated in terms of a fluidity tensor which quantifies how the fabric results in a different softness of ice for different stress components. The new contribution here is to consider how the azimuthal cross-section of the fabric which is measured by the radar (expressed an azimuthal orientation, θ_G or θ_P, and strength, G or P, parameter) acts to bound the tensor elements. We consider a full-range of possible rheology that can be measured by the radar, which extends beyond the data set in this paper.

A variety of approaches have been developed to model the anisotropic rheology of polycrystalline ice and are reviewed by Gagliardini et al. (2009). In the tensorial model used here, the polar ice is assumed to behave as linearly viscous orthotropic material (a class of anisotropic material where the mechanical properties are symmetrical with respect to three orthogonal planes) (Gagliardini & Meyssonnier, 1999; Gillet-chaulet et al., 2005; Martin et al., 2009). Anisotropy in the bulk rheology arises due to a combination of mechanical anisotropy at crystal scale (assumed model parameters) and anisotropy due to the ice fabric (the radar measurements). The crystal-scale anisotropy is parameterized via two ratios: (1) the viscosity of the grain for shear parallel to the basal plane to that in the basal plane, and (2) the ratio of the viscosity in compression or tension along the c-axis to that in the basal plane. We assume, following (Martin et al., 2009), that $\beta = 10^{-2}$ and $\gamma = 1$.

We follow the presentation of the model in the Appendix of Martin et al. (2009), based on (Gillet-chaulet et al., 2005) and (Gagliardini & Meyssonnier, 1999). In the orthotropic reference frame (the eigenvectors x_1, x_2, x_3 of $\mathbf{a}$) the strain, $\mathbf{D}$, and deviatoric stress, $\bar{\boldsymbol{S}}$, tensors can be written as 6-component vectors which are connected

via the matrix equation

$$\begin{pmatrix} D_{11} \\ D_{22} \\ D_{33} \\ D_{12} \\ D_{13} \\ D_{23} \end{pmatrix} = \psi_0 \begin{pmatrix} \psi_{1111} & \psi_{1122} & \psi_{1133} & 0 & 0 & 0 \\ \psi_{1122} & \psi_{2222} & \psi_{2233} & 0 & 0 & 0 \\ \psi_{1133} & \psi_{2233} & \psi_{3333} & 0 & 0 & 0 \\ 0 & 0 & 0 & \psi_{1212} & 0 & 0 \\ 0 & 0 & 0 & 0 & \psi_{1313} & 0 \\ 0 & 0 & 0 & 0 & 0 & \psi_{2323} \end{pmatrix} \begin{pmatrix} \bar{S}_{11} \\ \bar{S}_{22} \\ \bar{S}_{33} \\ \bar{S}_{12} \\ \bar{S}_{13} \\ \bar{S}_{23} \end{pmatrix}, \tag{5}$$

where $\boldsymbol{\psi}$ is the fourth-order fluidity tensor (inverse of the fourth-order viscosity tensor) and ψ_0 is a constant. The elements of $\boldsymbol{\psi}$ represent the relative softness of each deformation mode with respect to a random/isotropic fabric, whereby values greater than one indicate anisotropic ice that is softer than isotropic ice to an applied stress component.

In the general case, $\boldsymbol{\psi}$ is a function of β, γ, the second-order orientation tensor $\mathbf{a}$ and a fourth-order fabric orientation tensor, $\mathbf{a}^4$ (see Martin et al. (2009) equation (C1)). We cannot, however, uniquely measure the elements of $\mathbf{a}^4$ with radar. Following (Gillet-chaulet et al., 2005) we use a polynomial expansion to express $\mathbf{a}^4$ in terms of the eigenvalues a_1, a_2 and a_3. We then use the GP decomposition outlined in Section 3.3 to model the elements of $\boldsymbol{\psi}$ as a function of the two degrees of freedom G and P.

As described in Section 3.2, nadir radar-sounding may be used to estimate either G (vertical girdle strength where x_3 is assumed vertical) or P (horizontal pole strength where x_1 is assumed vertical). The radar can therefore constrain whatever elements of the fluidity tensor are assumed to be horizontal. Under the girdle assumption ψ_{1111}, ψ_{2222}, and ψ_{1212} are the horizontal uniaxial and lateral shear elements. Under the pole assumption ψ_{2222}, ψ_{3333}, and ψ_{2323} are the horizontal uniaxial and lateral shear elements.

A non-linear extension of equation (5) is considered by Martin et al. (2009) which mimics the n=3 power-law dependence of the commonly-used Glen's flow-law (Glen, 1954). Consequently, whilst we focus on a linear anisotropic rheology in this study, the radar measurements could also be used to parameterize a non-linear anisotropic flow law.

5.2 Anisotropic rheology for a non-ideal vertical girdle (x_3 vertical)

We first consider the anisotropic rheology of a vertical girdle fabric in the principal coordinate system (which, in general, is not aligned with the ice-flow coordinates). Fluidity elements ψ_{1111}, ψ_{2222}, and ψ_{1212} are shown as a function of P and G in Figures 5a and 5b. The uniaxial elements have approximately vertical contours with ψ_{1111} decreasing as G increases (i.e. girdle ice is harder than isotropic ice for compression/extension orthogonal to the girdle plane) and ψ_{2222} increasing as G increases (i.e. girdle ice is softer than isotropic ice for compression/extension parallel to the girdle plane). The lateral shear element, ψ_{1212}, Figure 5c has horizontal contours (i.e. it is a function of P and therefore cannot be constrained with the radar if it is assumed that a vertical girdle is being measured). For a given measurement of G, the pole strength bounds, P_{min} and P_{max} (Figure 2), are used as bounds for each element of $\boldsymbol{\psi}$.

To model the fluidity tensor in the ice-flow coordinates we use the following azimuthal rotation transformation

$$\boldsymbol{\psi}_{xyz} = K^{-T}(\theta_G - \theta_x)\boldsymbol{\psi}_{123}K^{-1}(\theta_G - \theta_x), \tag{6}$$

where $\boldsymbol{\psi}_{xyz}$ and $\boldsymbol{\psi}_{123}$ notate the fluidity tensor in the ice-flow and principal coordinate systems, K is a 6×6 rotation matrix, with K^{-1} the inverse matrix and K^{-T} the inverse-transpose matrix (refer to Ting (1996) for derivation and definitions). The rotation angle is defined such that when $(\theta_G - \theta_x) = 0°$, x_2 is aligned with x (i.e. the girdle plane is aligned with ice flow). Figures 5d-f show the uniaxial strain elements in the ice-flow coordinates, ψ_{xxxx} and ψ_{yyyy}, for a series of azimuthal girdle rotations. The rotation results in the hard (x_1) and soft (x_2) strain directions changing with respect to ice-flow direction. We do not show results for ψ_{xyxy} as there is only minor azimuthal variation from ψ_{1212} (Figure 5c).

The result that vertical girdle fabrics lead to anisotropic rheology for horizontal uniaxial strain is important for regions of the ice stream where extension and compression dominate over shear. Using the same flow-law as this study, Ma et al. (2010) demonstrated that extensional ice-shelf flow (where a girdle is anticipated to develop transverse to the flow-direction) leads to a relative hardening of the ice in the flow direction, consistent with Figure 5a. Additionally, the previous rheological model by van der Veen and Whillans (1994) predicts that girdle ice is softer than isotropic ice for compression in the girdle plane, consistent with Figure 5b. In the data analysis,

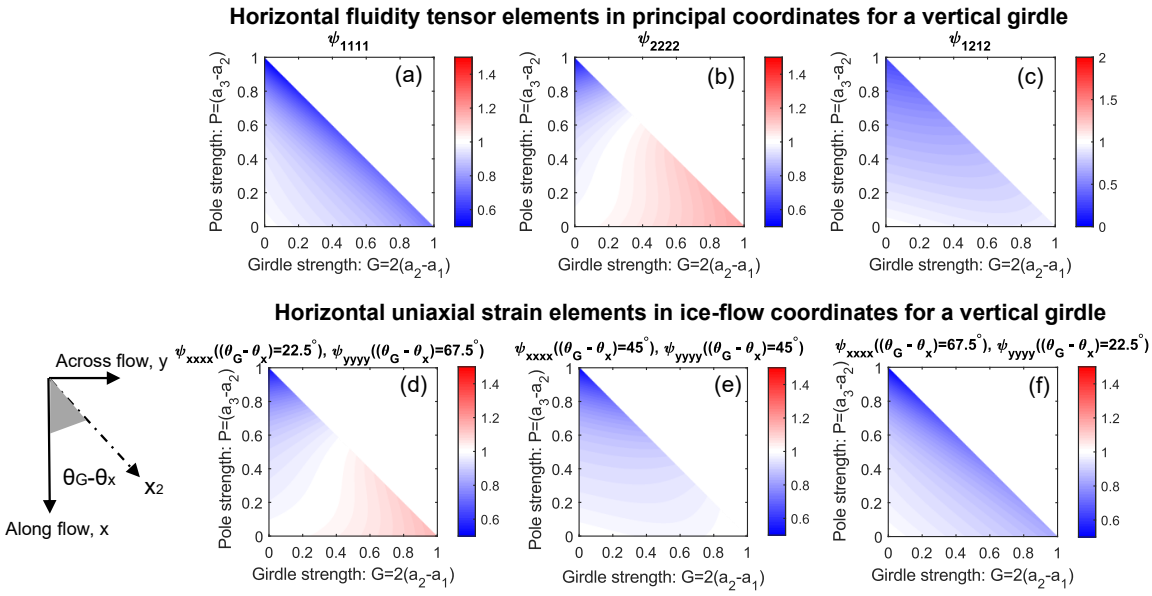

Figure 5. Top row: Horizontal elements of principal fluidity tensor for a non-ideal vertical girdle fabric (x_3 vertical). (a) ψ_{1111}, (b) ψ_{2222}, (c) ψ_{1212}. Bottom row: Horizontal uniaxial elements of fluidity tensor in ice-flow coordinates. (d) $\psi_{xxxx}((\theta_G - \theta_x) = 22.5°)$, (e) $\psi_{xxxx}((\theta_G - \theta_x) = 45°)$, (f) $\psi_{xxxx}((\theta_G - \theta_x) = 67.5°)$. Fluidity values greater than one indicate that anisotropic ice is softer than isotropic ice. When $(\theta_G - \theta_x)$=0°, $\psi_{2222} = \psi_{xxxx}$.

anisotropic rheology is quantified using fluidity tensor element ratios in the ice-flow coordinates (E. C. Smith et al., 2017). Specifically, we consider ψ_{xxxx}/ψ_{yyyy} (relative anisotropy of along-flow to across-flow uniaxial deformation), ψ_{xxxx}/ψ_{xyxy} (relative anisotropy of along-flow to lateral shear deformation). The ratios are computed by inputting the estimates and uncertainties for $(\theta_G - \theta_x)$ and G into the rheological model and then evaluating for the upper and lower pole bounds, P_{max} and P_{min} as described in Section 3.3. For an ideal vertical girdle (G=1, P=0) aligned with the flow direction $(\theta_G - \theta_x = 0°)$, the element ratios are given by $\psi_{xxxx}/\psi_{yyyy} = \psi_{2222}/\psi_{1111} \approx 1.61$ and $\psi_{xxxx}/\psi_{xyxy} = \psi_{2222}/\psi_{1212} \approx 2.11$.

5.3 Anisotropic rheology for a non-ideal horizontal pole (x_1 vertical)

Horizontal fluidity tensor elements in the principal coordinates for a horizontal pole are shown in Figure 6 (top row). Both ψ_{3333} and ψ_{2323} (now considered as horizontal elements) have a tendency toward vertical contours in GP space, and can therefore be constrained by measurements of P. Of particular note, the lateral shear element ψ_{2323} is softer relative to isotropic ice. The strong enhancement of ψ_{2323} for the single pole fabric (P=1, G=0) is better-known in the context of enhancing horizontal shear for a vertical single pole (Azuma & Goto-Azuma, 1996; Ma et al., 2010). Similarly, evaluating ψ_{3333} for(P=1, G=0) reproduces a standard result that single-pole ice becomes harder to uniaxial strain in the direction of the c-axes (Azuma & Goto-Azuma, 1996; Thorsteinsson et al., 1997).

To reference the pole to ice flow we use the angle $(\theta_P - \theta_x)$ which equals 0° when x_3 is aligned with ice-flow. An analogous rotation transformation to equation (6) can then be applied to calculate horizontal fluidity tensor elements for the horizontal pole in the ice-flow coordinates. The lateral shear element exhibits the greatest angular sensitivity, and Figure 6 (bottom row) shows ψ_{xyxy} as a function of $(\theta_P - \theta_x)$. Of particular note, is the result that a non-ideal horizontal pole ($P \approx 0.5$ or less) becomes softer to lateral shear as the x_3 axis rotates from 0° to 45° to flow. This result is crucial to understand the fabric estimates in the ice-stream margin region, and to the best of our knowledge has not previously been described.

To quantify the anisotropic rheology for the horizontal pole, fluidity tensor element ratios were evaluated for estimates of $(\theta_P - \theta_x)$ and P for upper and lower girdle

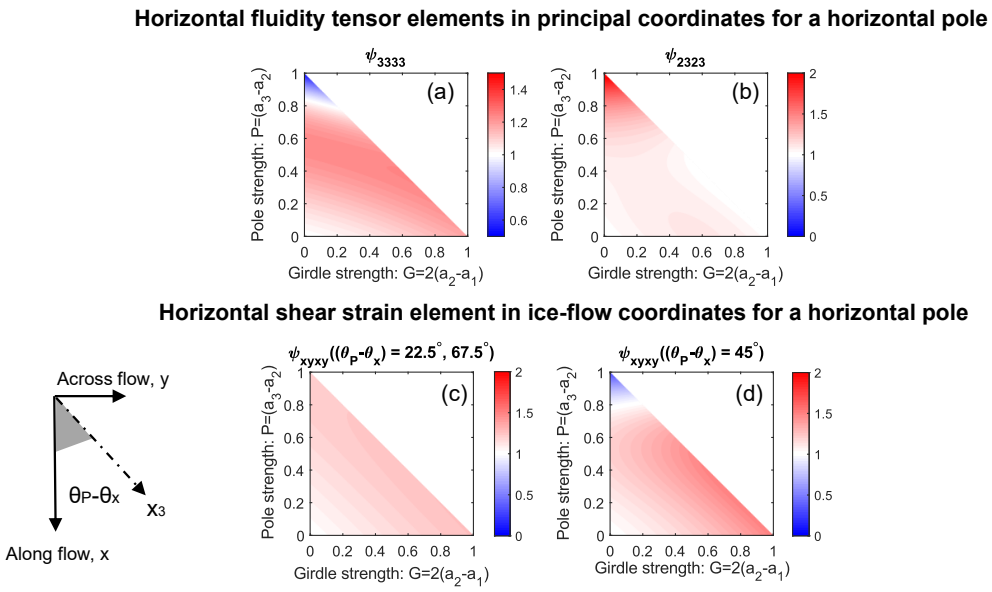

Figure 6. Top row: Horizontal elements of principal fluidity tensor for a horizontal pole fabric (x_1 vertical): (a) ψ_{3333}, (b) ψ_{2323}. Bottom row: lateral shear elements of fluidity tensor in ice-flow coordinates. (c) $\psi_{xyxy}((\theta_P - \theta_x) = 22.5°)$. (d) $\psi_{xyxy}((\theta_P - \theta_x) = 45°)$. When $(\theta_P - \theta_x)$=0°, $\psi_{2323} = \psi_{xyxy}$. ψ_{2222} is shown in Figure 5b.

bounds, G_{max} and G_{min}. These bounds correspond to the girdle strengths which maximize and minimize the anisotropy, which at lower values of $(\theta_P - \theta_x)$ can differ from the maximum and minimum girdle strengths due to the shape of the contours in GP space (eg. Figure 6b). The maximal shear-enhancement at 45° corresponds to $\psi_{xyxy}/\psi_{xxxx} \approx 1.60$, which occurs for the G_{max} bound (in this case the maximum girdle strength) of a non-ideal pole ($P \approx$ 0.2-0.5).

6 Results

6.1 Characterization of the ice-surface strain field

To place the ice fabric measurements in the context of ice deformation, we first characterize the ice-surface strain field of Rutford Ice Stream. The strain rates in the ice-flow coordinates, D_{xx}, D_{yy}, D_{xy} are shown in Figure 7a-c. The log-ratio, $\log_{10} \frac{|D_{xx}|}{|D_{xy}|}$, is used to quantify the magnitude of along-flow strain to lateral shear strain, Figure 7d. Lateral shear dominates over horizontal uniaxial strain toward the ice-stream margin whereas toward the center of the ice stream, along-flow uniaxial strain typically dominates over lateral shear. In the center of the ice stream there is a transition between compression and extension directions. Specifically, the 'downstream central region' (sites A1-A3 and sites B1-B2) corresponds to weak along-flow compression/across-flow extension, whereas the 'upstream central region' (sites B6-B10) corresponds to along-flow compression/across-flow extension.

The minimum horizontal strain rate (principal compression), D_{min} increases in magnitude toward the ice-stream margins, Figure 7e. The angle at which this principal compression acts is referenced to ice flow using $(\theta_{min} - \theta_x)$ where θ_{min} and θ_x are azimuthal bearing angles of the compression and flow axes, Figure 7f. (An upstream convention is assumed so that $0 \leq \theta_x < 180°$). $(\theta_{min} - \theta_x) = 0°$ corresponds to along-flow compression (approximately the case for the downstream region in the ice-stream center) and $(\theta_{min} - \theta_x) = \pm\, 90°$ corresponds to across-flow compression (approximately for the upstream region). When the ice flow is dominated by lateral shear it is a general result that $|\theta_{min} - \theta_x| \longrightarrow 45°$. This tendency can be understood from evaluating the principal (Mohr) angle formula

$$\theta_{min} = \frac{1}{2} \arctan \left(\frac{2D_{xy}}{(D_{xx} - D_{yy})} \right), \tag{7}$$

when $2|D_{xy}| >> |D_{xx} - D_{yy}|$.

The uncertainty and fractional uncertainty on the minimum principal strain, D_{min} are shown in Figures 7g and 7h, with the fractional uncertainty being appreciable (> 0.5) in the central region of Transect A and downstream region of Transect B. The uncertainty on $(\theta_{min} - \theta_x)$ is also highest ($\approx 30°$) in these regions, Figure 7i. Uncertainty in the ice-flow strain rates is comparable to D_{min}. The results in Figure 7a-c are qualitatively comparable to Minchew et al. (2016) (see their S18) but differ

quantitatively due to the resolution of the respective velocity fields and derivative procedures.

6.2 Estimation of ice fabric from the polarimetric coherence

For simplicity, in the polarimetric data analysis we describe the measured fabric as a vertical girdle (rather than a horizontal pole) by default. The vertical girdle model is anticipated to apply for the majority of the survey points (central region of Transect A and Transect B), with the horizontal pole model anticipated to apply to just the marginal region of Transect A.

Polarimetric coherence analysis results for three measurement sites along Transect A are shown in Figure 8 (refer to Supporting Information, Figures S2 and S3, for additional sites). A consistent feature is a band of high coherence magnitude, $|c_{hhvv}|$, in shallower ice which extends to z $\approx$ 160 m in the center of the ice stream (site A1) and z $\approx$ 80m toward the ice-stream margin (site A9). Therefore, to compare fabric estimates between sites we focus on $40 < z < 80$ m which we refer to as unit U1, indicated in Figure 8c.

Within U1, ϕ_{hhvv} and $d\phi_{hhvv}/dz$ are well-approximated by the backscatter simulation for depth-invariant principal axes, Figure 4a. A relative counter-clockwise rotation of θ_G occurs between the center of the ice stream (Site A1: $\theta_G \approx 85°$ in U1) and closest to the ice-stream margin (Site A9: $\theta_G \approx 140°$ in U1). The girdle strength generally increases toward the ice-stream margin, which is illustrated by the increasingly shallow depths of the first half-phase cycle ($\phi_{hhvv} = \pi$). At site A1, Figure 8a, there is evidence for azimuthal fabric rotation within the ice column, with θ_G in deeper ice rotated in a clockwise direction relative to ice in U1.

Polarimetric coherence analysis results for three measurement sites along Transect B are shown in Figure 9 (refer to Supporting Information, Figures S4 and S5, for additional sites). The high-coherence band along Transect B is generally deeper than along Transect A, and extends to $z \approx 160$ m or greater at all measurement sites. For $z < 160$ m, sites B1-B6 are qualitatively similar to site A1 (directly downstream along the center streamline) and approximate the backscatter simulations for depth-invariant principal axes, Figure 4a.

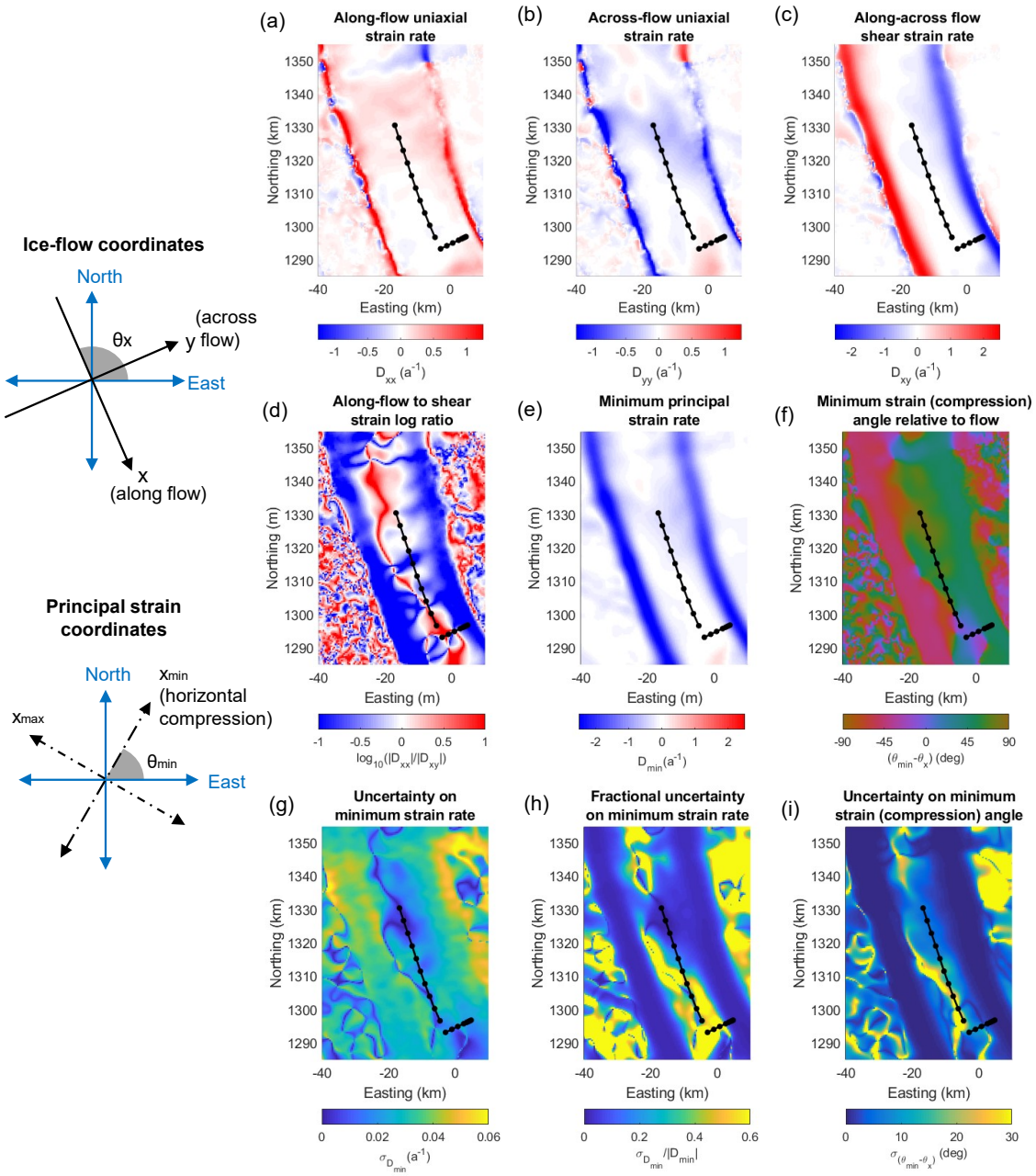

Figure 7. Characterization of the ice-surface strain field. (a) Uniaxial strain rate along ice flow. (b) Uniaxial strain rate across ice flow. (c) Lateral shear strain rate in ice-flow coordinates. (d) Along-flow to lateral shear strain log-ratio. (e) Minimum principal strain rate (horizontal compression). (f) Azimuthal angle of minimum strain (horizontal compression) relative to ice flow. (g) Uncertainty on minimum strain. (h) Fractional uncertainty on minimum strain. (i) Uncertainty on minimum strain angle relative to ice flow. Schematics for the ice-flow coordinates (x, y) and the principal strain coordinates (x_{min}, x_{max}) are shown.

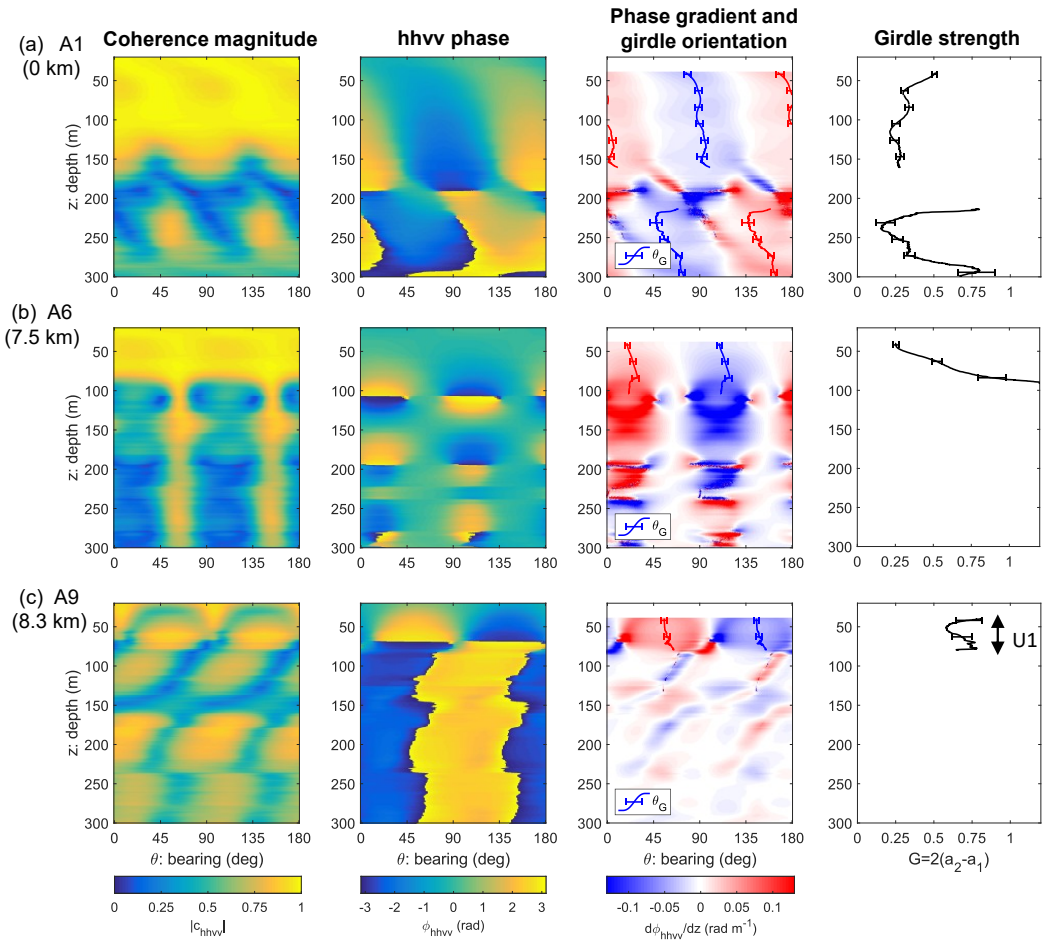

Figure 8. Polarimetric coherence analysis at three measurement sites along Transect A: (a) A1, (b) A6, (c) A9. The depth-profiles for the girdle fabric estimates, $\theta_G(z)$ and $G(z)$ are shown in the center right and far right columns. A filtering step is applied such that fabric estimates require $|c_{hhvv}(\theta_G, z)| > 0.5$. The depth interval used to assess horizontal variation in ice fabric, U1, is shown in (c).

By contrast, sites B8-B10 show two distinct sub-units within the high coherence band (e.g. Figure 9c). These three sites all approximate the backscatter simulations for a 90° azimuthal rotation in ice fabric within the ice column (Figure 4b). The depth-transition between the two units is approximately at 100 m depth. To compare fabric estimates between sites we focus on two layers: $40 < z < 80$ m (U1, as defined for Transect A), and $120 < z < 160$ m (U2). The gap between U1 and U2 is set to the coherence window size of 40 m so as not to bias the girdle strength estimates. Within U1, there is evidence for a decrease in fabric strength toward the center of Transect B. Notably, Site B6 has a slower vertical phase cycle, which is further decreased at site B7 (see Supporting Information).

Sites A10 and B1 were not included in the data analysis as fabric estimates could not be obtained within the unit depth intervals. In general, the coherence magnitude is too low for the estimation of continuous ice fabric profiles for z ¿ 300m. The exception is a band of high coherence in deeper ice ($z > 1400$ m), where the $hhvv$ phase gradient is negligible (see Supporting Information, Figure S6). Due to a general increase in the vertical eigenvalue with ice depth, this deeper fabric is consistent with the presence of an azimuthally-symmetric vertical cluster.

6.3 Spatial variation in ice fabric

The azimuthal orientation of the fabric, (θ_G - θ_x), and principal compression, (θ_{min} - θ_x), relative to ice flow are shown for unit U1 in Transect A, Figure 10a. The comparison is made to test the hypothesis that the fabric is consistent with strain-induced development that matches the local ice flow. The compression angle rotates counter-clockwise from along-flow in the center of the ice stream (site A1) to 45° to flow toward the ice-stream margin (site A9). The girdle orientation is closely correlated with the compression angle, rotating counter-clockwise by approximately 55° between site A1 and A9. There is, however a small systematic offset, between the girdle and the compression angle (typically ≈ -10°). The fabric strength within U1 ranges from $G \approx 0.4$ at A1 to $G \approx 0.7$ at A9, Figure 10b. G generally increases as the compressive strain rate, D_{min}, decreases (or equivalently $|D_{min}|$ increases).

Synthetic c-axis distributions which illustrate the combined effect of fabric rotation and strengthening, are shown in Figure 10c. The c-axis distributions are better

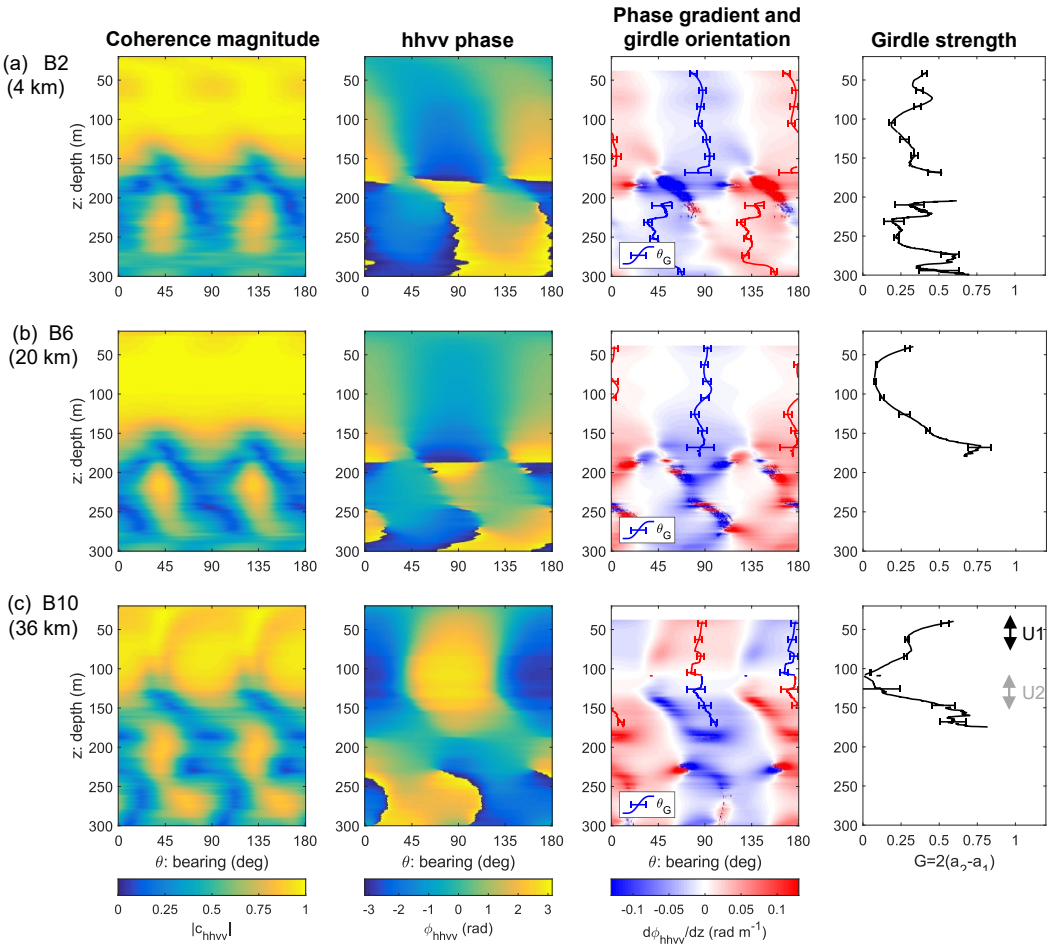

Figure 9. Polarimetric coherence analysis at three measurement sites along Transect B: (a) B2, (b) B6, (c) B10. The depth-profiles for the girdle fabric estimates, $\theta_G(z)$ and $G(z)$ are shown in the center right and far right columns. A filtering step is applied such that fabric estimates require $|c_{hhvv}(\theta_G, z)| > 0.5$. The black and grey arrows in (c) indicate the two units U1 and U2.

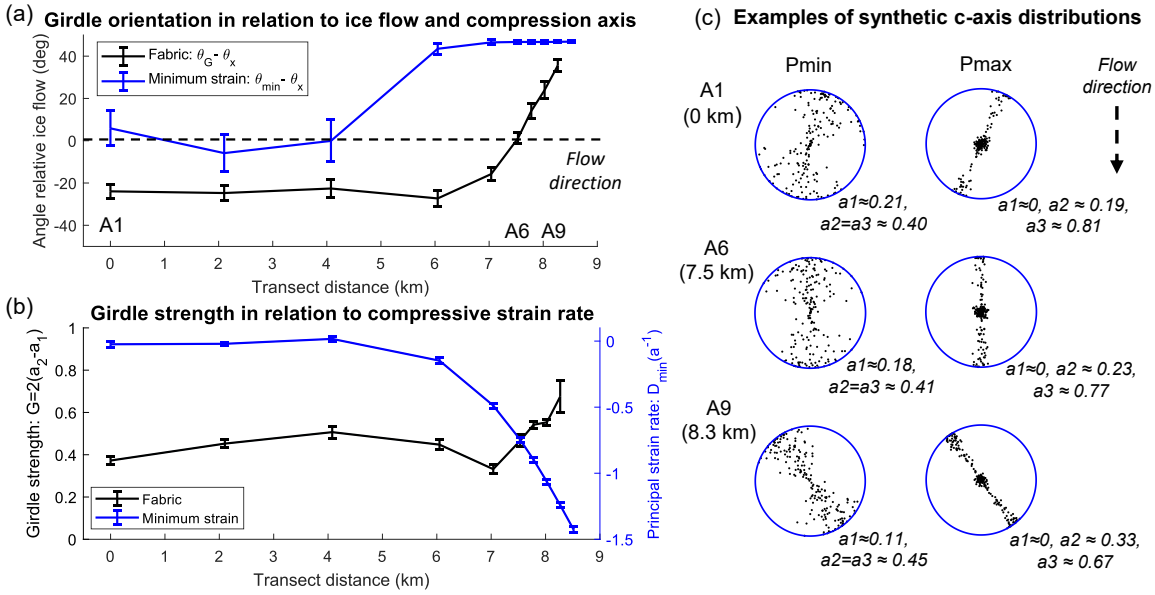

Figure 10. Spatial variation of ice fabric for unit U1 in Transect A. (a) Girdle orientation and horizontal compression axis relative to the ice-flow direction. (b) Girdle strength and principal compression magnitude. (c) Synthetic *c*-axis distributions for three measurement sites for the upper and lower pole bounds. The fabric estimates in U1 are depth-averaged over $40 < z < 80$ m. The visualization of the results assume a vertical girdle fabric (x_3 vertical). For a horizontal pole fabric (x_1 vertical), G is replaced by $\frac{P}{2}$ in (b) and $(\theta_G - \theta_x)$ is replaced by $(\theta_P - \theta_x)$ in (a).

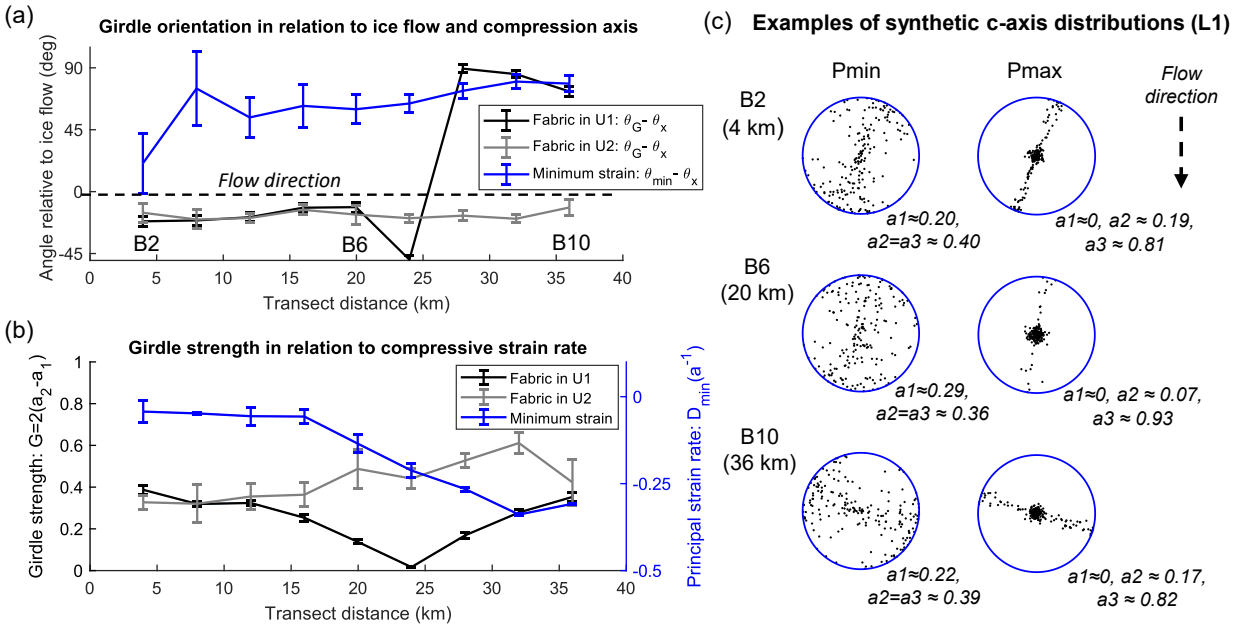

Figure 11. Spatial variation of ice fabric for unit U1 and U2 in Transect B. (a) Girdle orientation and horizontal compression axis relative to the ice-flow direction. (b) Girdle strength and principal compression magnitude. (c) Synthetic c-axis distributions for fabric in U1 at three measurement sites for the upper and lower pole bounds. The fabric estimates in U1 and U2 are depth-averaged over $40 < z < 80$ m and $120 < z < 160$ m respectively. The visualization of the results assume a vertical girdle fabric (x_3 vertical).

constrained toward the ice-stream margin where G is higher and the possible range for P is lower.

Fabric estimates for units U1 and U2 in Transect B are shown in Figures 11a and 11b along with synthetic c-axis distributions for U1 in Figure 11c. In general, $(\theta_G - \theta_x)$ is better correlated with $\theta_{min} - \theta_x$ in $U1$ than $U2$. Notably, at the upstream sites, B8-B10, the girdle and compression axes are both orientated across-flow, whereas, at the downstream site, B2, the girdle and compression axes are both orientated along-flow. However, both $(\theta_G - \theta_x)$ and G are less-well correlated with D_{min} than along Transect A, particularly when $|D_{min}|$ is low at sites B3-B7. In unit U2, θ_G and G are relatively constant along the entire length of Transect B, with the girdle orientated along-flow and $G \approx 0.4$-0.5.

6.4 Spatial variation in anisotropic rheology

The enhancements in fluidity assuming a vertical girdle (x_3 vertical) and horizontal pole (x_1 vertical) fabrics are compared for Transect A in Figure 12. In the center of the ice stream, where the vertical girdle assumption holds better, the ice is softer for along-flow deformation than across-flow deformation ($\psi_{xxxx}/\psi_{yyyy} > 1$) and softer for along-flow deformation than lateral shear ($\psi_{xxxx}/\psi_{xyxy} > 1$), Figures 12a and 12b. The uniaxial anisotropy in Figure 12(a) can be understood from Figures 5d-f since the girdle orientation is always closer to the along-flow than the across-flow direction ($|\theta_G - \theta_x| < 45°$). The maximum anisotropy, $\psi_{xxxx}/\psi_{yyyy} \approx 1.58$ and $\psi_{xxxx}/\psi_{xyxy} \approx 1.71$, occurs at site A6 when $|\theta_G - \theta_x|$ is closest to 0°. In the center of the ice stream, the horizontal pole model shows opposite behavior to the vertical girdle model ($\psi_{yyyy}/\psi_{xxx} > 1$ and $\psi_{xyxy}/\psi_{xxxx} > 1$), Figure 13.

In the ice-stream margins, where the horizontal pole assumption holds better, the ice is softer for lateral shear than along-flow deformation, ($\psi_{xyxy}/\psi_{xxxx} > 1$), Figure 12d. Furthermore, this shear-softening trend increases towards the margin. The shear enhancement at the margin can be understood from Figures 6b-d, as the fabric corresponds to a non-ideal horizontal pole (P≈ 0.25-35) being rotated away from $(\theta_P - \theta_x) \approx 0°$ (site A6) to $(\theta_P - \theta_x) \approx 35°$ (site A9). For the vertical girdle assumption, along-flow deformation is predicted to be softer than lateral shear near the ice stream margins ($\psi_{xxxx}/\psi_{xyxy} > 1$), Figure 12b.

In interpreting anisotropic rheology for Transect B, we always assume that the fabric is a vertical girdle (x_3 vertical). Unit U1 illustrates a spatial transition in anisotropic rheology, Figure 13c. For sites B2-B6 ice is softer in the along-flow direction ($\psi_{xxxx}/\psi_{yyyy} > 1$) whereas for sites B8-B10 ice is softer in the across-flow direction ($\psi_{xxxx}/\psi_{yyyy} < 1$) and qualitatively similar to Transect A (unit U1). The explanation for the different results at sites B8-B10 is that the girdle plane is closer to the across-flow than the along-flow direction ($|\theta_G - \theta_x| > 45°$). In Transect B (unit U1) ice is always softer for along-flow deformation relative to lateral shear ($\psi_{xxxx}/\psi_{xyxy} > 1$), Figure 13c. Transect B (U2), Figures 13e-f, illustrate very minor spatial variability in the rheology, with the ice always softer in the along-flow direction.

If a Glen-like n=3 rheology is considered then the anisotropic rheology increases following $(\psi_{xxxx}/\psi_{yyyy})^3$ and $(\psi_{xxxx}/\psi_{xyxy})^3$ (Martin et al., 2009; E. C. Smith et al.,

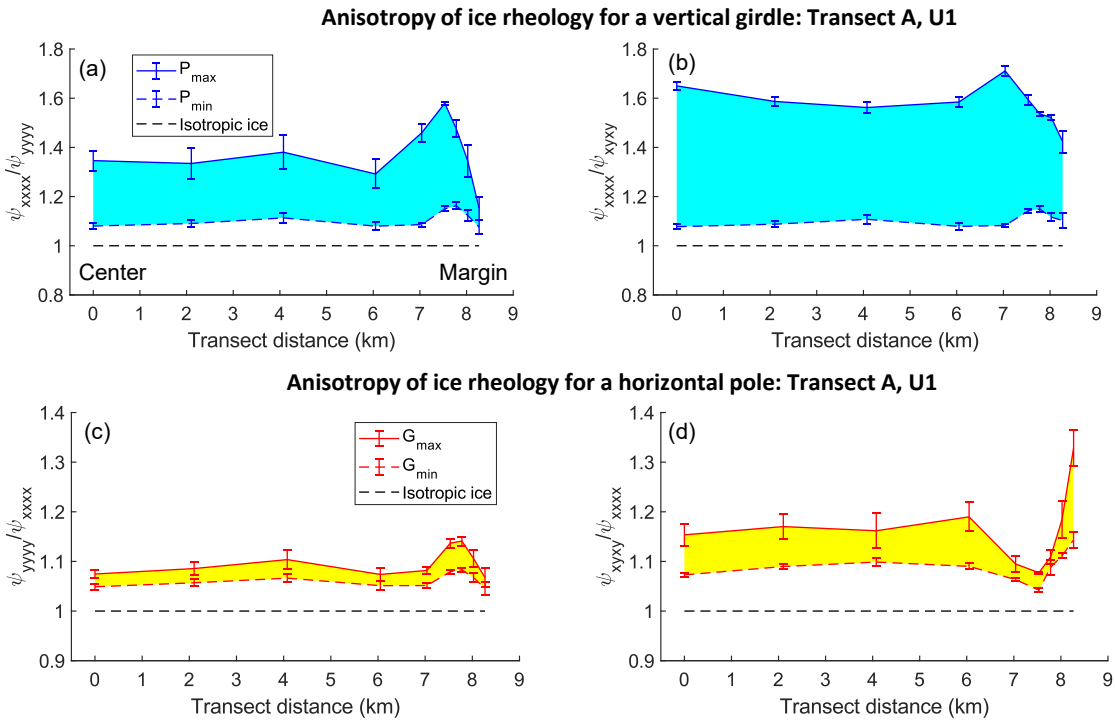

Figure 12. Bounds on the relative anisotropy of ice rheology for Transect A. Top row: (a) ψ_{xxxx}/ψ_{yyyy}, (b) ψ_{xxxx}/ψ_{xyxy} assuming a non-ideal vertical girdle (x_3 vertical). Bottom row: (c) ψ_{yyyy}/ψ_{xxxx}, (d) ψ_{xyxy}/ψ_{xxxx} assuming a non-ideal horizontal pole (x_1 vertical). The shaded regions correspond to values consistent with the pole/girdle bounds. The fluidity ratios are defined differently for the vertical girdle and the horizontal pole models, so as to emphasize which deformation mode is enhanced.

2017). Consequently, the upper estimates for linear anisotropy in Figure 12 and 13 change from ≈ 1.4-1.8 to 2.7-5.8 for non-linear anisotropy. Non-linearity also results in the difference between the upper and lower pole bounds increasing (the shaded regions in Figure 12 and 13).

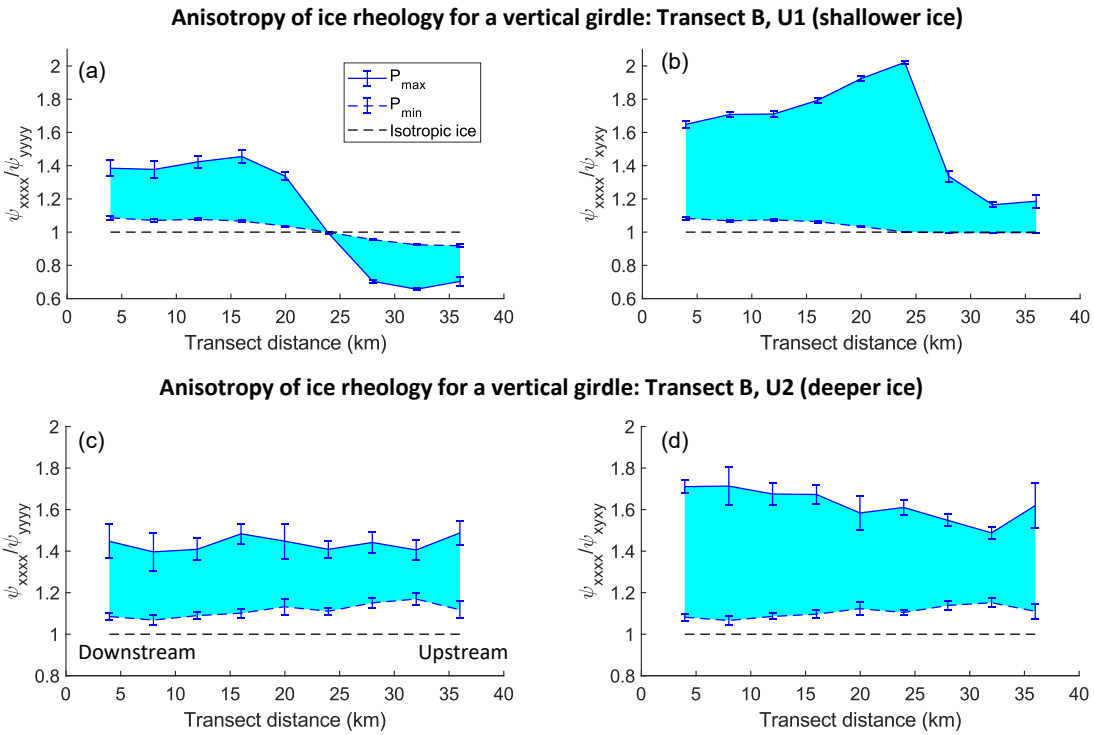

Figure 13. Bounds on the relative anisotropy of ice rheology for Transect B. Top row: (a) ψ_{xxxx}/ψ_{yyyy}, (b) ψ_{xxxx}/ψ_{xyxy} for unit U1. Bottom row: (c) ψ_{xxxx}/ψ_{yyyy}, (d) ψ_{xxxx}/ψ_{xyxy} for unit U2. All panels assume a non-ideal vertical girdle (x_3 vertical). The shaded regions correspond to values consistent with the pole bounds.

7 Discussion

7.1 Flow-induced fabric development in ice streams

Our data in shallow ice within Rutford Ice Stream (unit U1), generally show a strong correlation between crystal c-axis preferred orientations and the compressive strain direction, Figures 10a and 11a. This relationship has been predicted for flow-induced fabric, also known as strain- or dynamically-induced fabric, (Azuma & Higashi, 1985; Alley, 1988) and observed across various flow regimes across the ice sheets (e.g. Thorsteinsson et al. (1997); Wang et al. (2002); K. Matsuoka et al. (2012); Brisbourne et al. (2019); Jordan, Schroeder, et al. (2020)). Our shallow-ice data establishes that surface strain is the dominant mechanism to induce fabric where there is rapid local horizontal variation (length-scales < 5 km) in the compression axis. Most notably, Transect A results illustrate that the azimuthal compression and fabric orientation both rotate towards 45° relative to ice flow near the ice-stream margin, Figure 10a. Transect B illustrates that the fabric in the center of the ice stream also responds to local changes in the compression axis, with the upstream region corresponding to across-flow compression and fabric orientation and the downstream region (nearest to Transect A) corresponding to along-flow compression and fabric orientation, Figure 11a.

The correlation strength between the orientation of the shallow-ice fabric and the compression angle generally increases with the compressive strain rate, as does the azimuthal strength of the fabric, Figures 10b and 11b. These observations suggest that larger strains, result in a faster rate of fabric development. However, the relatively coarse resolution of the strain-field (limited by the filter width in the spatial derivative) impedes a refined estimation of the length- and time-scales it takes for the fabric to develop.

An important caveat when interpreting our results is that the downstream region of the central ice stream (sites A1-A4 and B2) is an atypical deformation regime for an ice stream. Specifically, this region corresponds to relatively weak along-flow compression and across-flow extension, Figure 7. By contrast, the upstream region of Transect B is likely to be more representative, with along-flow extension and across-flow compression present. The azimuthal angle of principal compression that we observe in the ice-stream margins, $\pm$ 45° relative to ice flow, is anticipated to be a ubiquitous

property within ice streams. A physical way to understand this result is that it is the compression angle which corresponds to maximal lateral shear in the ice-flow coordinate system. Consequently, the tendency of the near-surface fabric to be at 45° to the shear plane is also expected to be common within ice streams. It has, however, been observed previously, near nunataks (protruding mountain peaks from a glacier), a tendency for the c-axes to rotate 90° to the shear plane (Fujita & Mae, 1994). This 90° orientation is consistent with an additional rigid-body rotation of the ice, as well as flow-induced development toward the compression axis (Alley, 1988). It is beyond the scope of our study to assess the relative contribution of flow and rotation mechanisms, but our observed fabric orientation implies flow-induced development is important near ice-stream margins.

7.2 The significance of azimuthal fabric rotation within the ice column

A particularly striking result from the radar fabric characterization is the azimuthal rotation of nearly 90° at depth within the ice column between units U1 and U2 at the upstream region of Transect B, Figure 9(c). A consequence of this azimuthal rotation is that the fabric orientation in deeper ice (unit U2, fabric orientation along ice flow) is significantly misaligned with the across-flow surface compression axis, Figure 11. Broadly analogous behavior (i.e. better alignment between surface compression and fabric in shallower ice than deeper ice) has been noted in other polarimetric radar-sounding studies, at ice divides (K. Matsuoka et al., 2012), ice rises (Brisbourne et al., 2019) and within Whillans Ice Stream (Jordan, Schroeder, et al., 2020).

For consistency with flow-induced fabric development, the fabric orientation in unit U2 implies that the ice is undergoing (or has undergone) along-flow compression. This assertion is backed-up by the presence of along-flow compression in the surface ice $\approx$ 20-30 km upstream of site B10, Figure 7. Significantly, this observation is consistent with the fabric in U2 developing upstream in the near-surface, then being horizontally and vertically advected to its current location. Alternatively, temporal changes in the surface strain field could contribute to the observed difference between the surface strain and unit U2. On a related note, the systematic offset between the fabric orientation and the compression axis for Transect A, Figure 10, could potentially be explained by either advection or temporal changes in the surface strain field.

An important consequence of azimuthal fabric rotation within the ice column is that it results in a depth-transition in the anisotropic rheology. Specifically, shallow ice (U1) is harder for along-flow strain than across flow, whereas the deeper ice (U2) is softer for across-flow strain, Figure 13. This result has particular significance for studies that use ice-surface strain information within inverse ice-sheet modeling (MacAyeal, 1992; Hindmarsh, 2004; Schoof & Hindmarsh, 2010; Goldberg, 2011). Specifically, the shallow depth of the fabric rotation ($\approx$ 100 m) indicates that there are circumstances when only the shallowest ice fabric and rheology is (directly) related to the local surface strain field.

7.3 The impact of ice fabric on anisotropic rheology and ice flow

The radar characterization of anisotropic rheology is dependent on whether azimuthal anisotropy is interpreted as a non-ideal vertical girdle (x_3 vertical) or a horizontal pole (x_1 vertical) fabric. Across the majority of the ice sheets, where horizontal strain rates are lower than at ice-stream margins, the vertical girdle interpretation is more likely to hold. This scenario likely applies to the central region of the ice stream (Transect B, and sites A1-A4). The rheology of the vertical girdle becomes important when the ice-flow deformation undergoes significant uniaxial strain, as can occur in the center of Rutford Ice Stream, Figure 7d. Significantly, the ice becomes softer in the direction of the girdle plane, which is correlated with the compression direction. In turn, this mechanism results in shallow ice (U1) in the upstream region being harder to along-flow than across-flow deformation, and vice-versa in the downstream region.

Toward the ice-stream margin (sites A5-A9), lateral shear strain dominates uniaxial strain, Figure 7d, and the horizontal pole (x_1 vertical) assumption is more likely to hold. Under this assumption, the softening of ice due to the non-ideal pole is consistent with Minchew et al. (2018) who predicted that ice fabric has a softening effect on ice rheology within the margins of Rutford Ice Stream. The softening effect reported by Minchew et al. (2018) was inferred from a combination of ice-surface remote sensing data and ice-flow modeling, rather than from direct measurements of ice fabric. It is important to note that an ideal single pole fabric, as hypothesized to exist by Minchew et al. (2018), would require the pole axis to be aligned either across or along-flow to optimally enhance lateral shear, Figure 6b. However, the azimuthal fabric orientation in the marginal region of Transect A is observed to be closer $\pm$ 45° to flow, and is

likely to be restricted to this orientation due to surface compression angle, Figure 7e. In this restricted scenario, the non-ideal horizontal pole (as is observed by the radar assuming x_1 is vertical) is a better enhancer of lateral shear than an ideal pole, Figure 6d.

A more general point to consider is the feedback between ice rheology and basal conditions in influencing the heterogeneity of the ice-surface deformation. Specifically, the alternating bands of along- and across- flow extension and compression in the center of Rutford Ice Stream, Figure 7, could arise primarily from an englacial viscous (regulatory) feedback mechanism. Under this interpretation, the girdle ice becomes harder in the extensional direction (Castelnau et al., 1996; Ma et al., 2010), acting to regulate strain rates in the direction of flow, and resulting in heterogeneity in the strain field (Ng, 2015). On the other hand, previous topographic (King et al., 2016) and seismic investigation (A. M. Smith, 1997) of Rutford Ice Stream have shown there to be distinct heterogeneity to the bed of the ice stream. This includes the presence of hard-bedded outcrops (King et al., 2016) and basal transitions between deforming and undeforming till (A. M. Smith, 1997). Since ice compression is enhanced by a girdle fabric, the ice rheology will act to enhance the compressing effect of basal obstacles and irregularities on the ice deformation.

7.4 Comparison with previous seismic measurements of fabric at Rutford Ice Stream

Previous studies of ice column fabric at Rutford Ice Stream, utilizing seismic shear-wave splitting observations (Harland et al., 2013; E. C. Smith et al., 2017), observe both vertical and azimuthal anisotropy. Both studies used icequakes from the bed of the ice stream (z> 2000 m) recorded at surface stations over a 10 km wide section of the central ice stream, in the vicinity of sites A1 and B2. The more comprehensive study of E. C. Smith et al. (2017) synthezised splitting observations with an average ice-column fabric combining an azimuthally symmetric vertical cluster and an azimuthally anisotropic 'horizontal partial girdle' (HPG), similar in form to the horizontal pole fabric presented here. The vertical cluster component, which relates to the strength of the vertical fabric eigenvalue, cannot be characterized with our radar method. However, the deeper-ice data (see Supporting Information, Figure S6)

supports that the cluster dominates at ice depth $z > 1400$ m, as there is no evidence for significant azimuthal anisotropy.

The shear-wave splitting method samples a column-averaged fabric between the ice stream bed and the surface. Under certain conditions, the method can be used to discriminate layered fabric structure. However, E. C. Smith et al. (2017) were unable to detect discrete layering in their observations and assumed a homogeneous anisotropic diffuse medium throughout the ice column. Both data sets indicate azimuthal anisotropy although there are differing orientations for the interpreted girdle fabric. Specifically, in this study unit U2 (deepest ice considered in this study over 120-160 m) the vertical girdle (x_2 axis) is aligned approximately parallel to flow. However, in the seismic interpretation of the full ice column by E. C. Smith et al. (2017), the x_2 axis of the bulk ice column is perpendicular to flow. Although we are unable to directly explain these discrepancies it is likely that a combination of the inherent spatial and depth averaging nature of the seismic method and a lower sensitivity to thin layers results in the small scale structure presented here being subsumed into a bulk fabric interpretation. We can, however, conclude that it is unlikely that U2 is representative of the rest of the ice column and a fabric more similar to that presented by E. C. Smith et al. (2017) is likely to dominate in deeper ice.

8 Summary and conclusions

In this study we use polarimetric radar sounding to investigate controls on the spatial development of ice crystal orientation fabric within the near-surface (top 40-300 m) of Rutford Ice Stream. We then use the radar fabric estimates to parameterize an anisotropic flow law and assess the impact of the fabric on ice flow. Our study reveals pronounced horizontal and depth-variation in both fabric and anisotropic rheology within the flow unit.

The main conclusions are:

1. *Near-surface fabric in ice streams is strain-induced by ice flow.*
   The radar characterization of azimuthal fabric anisotropy in the shallowest ice (top 40-100 m) is consistent with strain-induced development that correlates with present-day ice flow. This finding confirms expected behavior (correlation between the horizontal compression axis and direction of greatest horizontal *c*-

axis alignment), but also highlights that the fabric responds to locally-variable ($<$ 5 km scale) changes in the horizontal compression direction. Of particular note, at the ice-stream margins there is a tendency for the horizontal compression axis and the fabric to be oriented at 45° to the ice-flow direction, which is consistent with simple shear. In the ice-stream center the compression axis and the fabric can be orientated either along- or across-flow.

2. *Deeper ice-stream fabric can be significantly misaligned with the surface strain.* The radar measurements in the center of the ice stream show that in deeper ice (greater 100 m), the fabric can be azimuthally offset from the surface compression direction ($\approx 90°$ in extreme cases). Due to misalignment with the local strain field and alignment with the upstream strain field, our results suggest that ice-stream fabric is induced near the surface and preserved during downstream transport. Additionally, the results expose that, in some regions of ice streams, the ice-surface strain rates are likely to be a poor proxy for englacial strain-rates. This represents a new challenge for models that invert basal conditions and viscosity from surface strain-rates assuming simplified vertical variation of rheology.

3. *Ice-stream fabric can enhance both horizontal compression and lateral shear.* The rheological modeling illustrates that the changes in azimuthal fabric orientation and strength result in spatially-variable enhancement of lateral shear and uniaxial deformation with the ice stream. The details of these findings are, however, dependent on an assumption whether the fabric is a non-ideal vertical girdle (greatest c-axis alignment vertical) or a non-ideal horizontal pole (greatest c-axis alignment horizontal). Our first hypothesis is that the fabric in the center of the ice stream is a non-ideal vertical girdle that enhances horizontal compression. This girdle fabric will enhance the compression of ice due to basal obstacles, and is likely to play an important role in the regulation of ice-stream flow. Our second hypothesis is that the fabric in the ice-stream margin is a non-ideal horizontal pole that enhances lateral shear. This pole fabric will combine with strain heating to soften the marginal ice.

Appendix A Glossary of key symbols

A glossary of the key symbols used throughout this study is shown in Table A1.

Acknowledgments

Radar data were collected as part of the BEAMISH Project (NERC AFI award numbers NE/G014159/1 and NE/G013187/1). We are grateful to Rebecca Schlegel and Anne Flink for assistance with data acquisition. TMJ would like to acknowledge support from EU Horizons 2020 grant 747336-BRISRES-H2020-MSCA-IF-2016. DMS was supported, in part, by NSF CAREER Award 1745137. Polarimetric ApRES data are available via NERC's Polar Data Centre: https://doi.org/10.5285/D5B7E5A1-B04D-48D8-A440-C010658EC146. The MEaSURES ice velocity data products are available at NSIDC: https://nsidc.org/data/measures.

References

Alley, R. B. (1988). Fabrics in polar ice sheets: Development and prediction. *Science*, *240*(4851), 493–495. doi: 10.1126/science.240.4851.493

Azuma, N., & Goto-Azuma, K. (1996). An anisotropic flow-law for ice-sheet ice and its implications. *Annals of Glaciology*, *23*, 201–208. doi: https://doi.org/10.1016/0012-821X(94)90173-2

Azuma, N., & Higashi, A. (1985). Formation processes of ice fabric pattern in ice sheets. *Annals of Glaciology*, *6*, 130–134. doi: 10.3189/1985AoG6-1-130-134

Boerner, W. M. (1992). Basic concepts in radar polarimetry: Polsarpro v3.0. ESA Earth Online. Retrieved from `https://earth.esa.int/documents/653194/656796/LN_Advanced_Concepts.pdf` doi: doi:10.1029/96JB00412

Brennan, P. V., Lok, L. B., Nicholls, K., & Corr, H. (2014). Phase-sensitive FMCW radar system for high-precision Antarctic ice shelf profile monitoring. *IET Radar Sonar Navigation*, *8*(February 2013), 776–786. doi: 10.1049/iet-rsn.2013.0053

Brisbourne, A. M., Martin, C., Smith, A. M., Baird, A. F., Kendall, J. M., & Kingslake, J. (2019). Constraining Recent Ice Flow History at Korff Ice Rise, West Antarctica, Using Radar and Seismic Measurements of Ice Fabric. *Journal of Geophysical Research: Earth Surface*, *124*, 175-194-373. doi:

10.1029/2018JF004776

Budd, W. F., Warner, R. C., Jacka, T. H., Li, J., & Treverrow, A. (2013). Ice flow relations for stress and strain-rate components from combined shear and compression laboratory experiments. *Journal of Glaciology*, *59*(214), 374–392. doi: 10.3189/2013JoG12J106

Castelnau, O., Duval, P., Lebensohn, R. A., & Canova, G. R. (1996). Viscoplastic modeling of texture development in polycrystalline ice with a self-consistent approach: Comparison with bound. *Journal of Geophysical Research*, *101*(B6), 13851-13868. doi: 10.1029/96JB00412

Cuffey, K., & Paterson, W. S. B. (2010). The physics of glaciers, fourth edition. In (chap. 3). Academic Press.

Dall, J. (2009). Polarimetric ice sounding at p-band: First results. *IEEE 2009 International Geoscience and Remote Sensing Symposium (IGARSS 2009), Cape Town, July 2009*, 1024-1027.

Dall, J. (2010). Ice sheet anisotropy measured with polarimetric ice sounding radar. *30th International Geoscience and Remote Sensing Symposium (IGARSS 2010), 25–30 July 2010, Honolulu, HI, USA.*, 2507–2510.

Doake, C. S. M., Corr, H. F. J., Jenkins, A., Nicholls, K. W., & Stewart, C. (2003). Interpretation of polarization behaviour of radar waves transmitted through antarctic ice shelves. *Proceedings of the Workshop on POLinSAR - Applications of SAR Polarimetry and Polarimetric Interferometry (ESA SP-529)*, 1-8.

Faria, S. H., Weikusat, I., & Azuma, N. (2014). The microstructure of polar ice . Part II: State of the art. *Journal of Structural Geology*, *61*, 21–49. doi: 10.1016/j.jsg.2013.11.003

Fujita, S., & Mae, S. (1994). Strain in the ice sheet deduced from the crystal-orientation fabrics fro, bare icefields adjacent to the Sor-Rondane Mountains, Dronning Maud Land, East Antarctica. *Journal of Glaciology*, *40*(134), 135–139. doi: https://doi.org/10.3189/S0022143000003907

Fujita, S., Maeno, H., & Matsuoka, K. (2006). Radio-wave depolarization and scattering within ice sheets: a matrix-based model to link radar and ice-core measurements and its application. *Journal of Glaciology*, *52*(178), 407–424. doi: https://doi.org/10.3189/172756506781828548

Fujita, S., Maeno, H., Uratsuka, S., Furukawa, T., Mae, S., Fujii, Y., & Watanabe, O. (1999). Nature of radio echo layering in the Antarctic ice sheet detected by a two-frequency experiment. *Journal of Geophysical Research*, *104*(10), 13–13. doi: 10.1029/1999JB900034

Fujita, S., Matsuoka, T., Ishida, T., Matsuoka, K., & Mae, S. (2000). A summary of the complex dielectric permittivity of ice in the megahertz range and its applications for radar sounding of polar ice sheets. *Physics of Ice Core Records*, *104*, 185–212.

Gagliardini, O., Gillet-chaulet, F., & Montagnat, M. (2009). A Review of Anisotropic Polar Ice Models: from Crystal to Ice-Sheet Flow Models. *Low Temperature Science*, *68*, 149-166.

Gagliardini, O., & Meyssonnier, J. (1999). Analytical derivations for the behavior and fabric evolution of a linear orthotropic ice polycrystal. *Journal of Geophysical Research*, *104*, 17797-17809. doi: https://doi.org/10.1029/1999JB900146

Gillet-chaulet, F., Gagliardini, O., Meyssonnie, J., Montagnat, M., & Castelnau, O. (2005). A user-friendly anisotropic flow law for ice-sheet modelling. *Journal of Glaciology*, *51*(172), 3–14. doi: https://doi.org/10.3189/172756505781829

Glen, J. W. (1954). The creep of polycrystalline ice. *Proc. R. Soc. Lond. A*, *228*(1175), 519–538. doi: https://doi.org/10.1098/rspa.1955.0066

Godert, G. (2003). A mesoscopic approach for modelling texture evolution of polar ice including recrystallization phenomena. *Annals of Glaciology*, *37*, 1–28. doi: https://doi.org/10.3189/172756403781815375

Goldberg, D. N. (2011). A variationally derived, depth-integrated approximation to a higher-order glaciological flow model. *Journal of Glaciology*, *57*(201), 157–170. doi: 10.3189/002214311795306763

Graham, F. S., Morlighem, M., Warner, R. C., & Treverrow, A. (2018). Implementing an empirical scalar constitutive relation for ice with flow-induced polycrystalline anisotropy in large-scale ice sheet models. *The Cryosphere*, *12*, 1047–1067. doi: https://doi.org/10.5194/tc-12-1047-2018

Greene, C. A., Gwyther, D. E., & Blankenship, D. D. (2017, July). Antarctic mapping tools for matlab. *Comput. Geosci.*, *104*(C), 151–157. doi: 10.1016/j.cageo.2016.08.003

Harland, S., Kendall, J.-M., Stuart, G., Lloyd, G., Baird, A., Smith, A., ... Brisbourne, A. (2013). Deformation in Rutford Ice Stream, West Antarctica: measuring shear-wave anisotropy from icequakes. *Annals of Glaciology*, *54*(64), 105–114. doi: 10.3189/2013AoG64A033

Hindmarsh, R. C. A. (2004). A numerical comparison of approximations to the stokes equations used in ice sheet and glacier modeling. *Journal of Geophysical Research: Earth Surface*, *109*(F1). doi: 10.1029/2003JF000065

Horgan, H. J., Anandakrishnan, S., Alley, R. B., Burkett, P. G., & Peters, L. E. (2011). Englacial seismic reflectivity: Imaging crystal-orientation fabric in West Antarctica. *Journal of Glaciology*, *57*(204), 639–650. doi: https://doi.org/10.3189/002214311797409686

Jackson, M., & Kamb, B. (1997). The marginal shear stress of Ice Stream B, West Antarctica. *Journal of Glaciology*, *43*(145), 415–426. doi: https://doi.org/10.3189/S0022143000035000

Jordan, T. M., Besson, D. Z., Kravchenko, I., Latif, U., Madison, B., Nokikov, A., & Shultz, A. (2020). Modeling ice birefringence and oblique radio wave propagation for neutrino detection at the south pole. *Annals of Glaciology*, *61*(81), 84–91. doi: 10.1017/aog.2020.18

Jordan, T. M., Schroeder, D. M., Castelletti, D., Li, J., & Dall, J. (2019). A Polarimetric Coherence Method to Determine Ice Crystal Orientation Fabric From Radar Sounding: Application to the NEEM Ice Core Region. *IEEE Transactions on Geoscience and Remote Sensing*, 1–17. doi: 10.1109/TGRS.2019.2921980

Jordan, T. M., Schroeder, D. M., Elsworth, C. W., & Siegfried, M. R. (2020). Estimation of ice fabric within whillans ice stream using polarimetric phase-sensitive radar sounding. *Annals of Glaciology*, *61*(81), 74–83. doi: 10.1017/aog.2020.6

King, E. C., Pritchard, H. D., & Smith, A. M. (2016). Subglacial landforms beneath Rutford Ice Stream, Antarctica: detailed bed topography from ice-penetrating radar. *Earth System Science Data*, *8*, 151–158. doi: 10.5194/essd-8-151-2016

Kluskiewicz, D., Waddington, E. D., Anandakrishnan, S. ., Voigt, D. E., Matsuoka, K., & McCarthy, M. P. (2017). Sonic methods for measuring crystal orientation fabric in ice, and results from the West Antarctic Ice Sheet (WAIS)

Divide. *Journal of Glaciology*, *63*(240), 603–617. doi: 10.1017/jog.2017.20

Li, J., González, J. A. V., Leuschen, C., Harish, A., Gogineni, P., Montagnat, M., ... Paden, J. (2018). Multi-channel and multi-polarization radar measurements around the NEEM site. *The Cryosphere*, *12*, 2689–2705. doi: https://doi.org/10.5194/tc-12-2689-2018

Ma, Y., Gagliardini, O., Ritz, C., Gillet-chaulet, F., & Montagnat, M. (2010). Enhancement factors for grounded ice and ice shelves inferred from an anisotropic ice-flow model. *Journal of Glaciology*, *56*(199), 805–812. doi: https://doi.org/10.3189/002214310794457209

MacAyeal, D. R. (1992). The basal stress-distribution of Ice Stream-E, Antarctica, inferred by control methods. *Journal of Geophysical Research*, *97*(B1), 595–603. doi: https://doi.org/10.1029/91JB02454

Martin, C., Gudmundsson, G. H., Pritchard, H. D., & Gagliardini, O. (2009). On the effects of anisotropic rheology on ice flow, internal structure, and the age-depth relationship at ice divides. *Journal of Geophysical Research: Earth Surface*, *114*(4), 1–18. doi: 10.1029/2008JF001204

Matsuoka, K., Power, D., Fujita, S., & Raymond, C. F. (2012). Rapid development of anisotropic ice-crystal-alignment fabrics inferred from englacial radar polarimetry, central West Antarctica. *Journal of Geophysical Research: Earth Surface*, *117*(3), 1–16. doi: 10.1029/2012JF002440

Matsuoka, K., Wilen, L., Hurley, S., & Raymond, C. (2009, may). Effects of Birefringence Within Ice Sheets on Obliquely Propagating Radio Waves. *IEEE Transactions on Geoscience and Remote Sensing*, *47*(5), 1429–1443. doi: 10.1109/TGRS.2008.2005201

Matsuoka, T., Fujita, S., & Mae, S. (1996). Effect of temperature on dielectric properties of ice in the range 5−39 ghz. *Journal of Applied Physics*, *80*(109). doi: 10.1063/1.363582

Minchew, B. M., Meyer, C. R., Robel, A. A., Gudmundsson, G. H., & Simons, M. (2018). Processes controlling the downstream evolution of ice rheology in glacier shear margins: case study on Rutford Ice Stream, West Antarctica. *Journal of Glaciology*, *64*(248), 583–594. doi: 10.1017/jog.2018.47

Minchew, B. M., Simons, B., Riel, & Milillo, P. (2016). Tidally induced variations in vertical and horizontal motion on Rutford Ice Stream , West Antarctica,

inferred from remotely sensed observations. *Journal of Geophysical Research: Earth Surface*, *122*, 167–190. doi: 10.1002/2016JF003971

Montagnat, M., Azuma, N., Eichler, J., Fujita, S., Kipfstuhl, S., & Samyn, D. (2014). Fabric along the NEEM ice core, Greenland, and its comparison with GRIP and NGRIP ice cores. *The Cryosphere*, *8*, 1129–1138. doi: 10.5194/tc-8-1129-2014

Ng, F. (2015). Spatial complexity of ice flow across the Antarctic Ice Sheet. *Nature Geoscience*, *8*, 847-–850. doi: https://doi.org/10.1038/ngeo2532

Nicholls, K. W., Corr, H. F. J., Stewart, C. L., Lok, L. B., Brennan, P. V., & Vaughan, D. G. (2015). Instruments and Methods A ground-based radar for measuring vertical strain rates and time-varying basal melt rates in ice sheets and shelves. *Journal of Glaciology*, *61*(230), 1079–1087. doi: 10.3189/2015JoG15J073

Pettit, E. C., Thorsteinsson, T., Jacobson, H. P., & Waddington, E. D. (2007). The role of crystal fabric in flow near an ice divide. *Journal of Glaciology*, *53*(181), 277–288. doi: https://doi.org/10.3189/172756507782202766

Picotti, S., Vuan, A., Carcione, J. M., Horgan, H. J., & Anandakrishnan, S. (2015). Anisotropy and crystalline fabric of Whillans Ice Stream (West Antarctica) inferred from multicomponent seismic data. *Journal of Geophysical Research: Solid Earth*, *120*, 4237–4262. doi: 10.1002/2014JB011591

Rignot, E., Mouginot, J., & Scheuchl, B. (2011). Ice Flow of the Antarctic Ice Sheet. *Science*, *33*(6048), 1427–1430. doi: 10.1126/science.1208336

Rignot, E., Mouginot, J., & Scheuchl, B. (2017). *MEaSUREs InSARBased Antarctica Ice Velocity Map, Version 2, Boulder, Colorado USA, NASA National Snow and Ice Data Center Distributed Active Archive Center, https://doi.org/10.5067/D7GK8F5J8M8R, 2017.*

Rongen, M. (2019). Sampling c-axes distributions from the eigenvalues of ice fabric orientation tensors. *The Cryosphere Discussions*(November), 1–7. doi: https://doi.org/10.5194/tc-2019-204

Schoof, C., & Hindmarsh, R. C. A. (2010). Thin-film flows with wall slip: an asymptotic analysis of higher-order flow models. *The Quarterly Journal of Mechanics and Applied Mathematics*, *63*(1), 73-114. doi: 10.1093/qjmam/hbp025

Smith, A. M. (1997). Basal conditions on rutford ice stream, west antarctica, from

seismic observations. *Journal of Geophysical Research: Solid Earth*, *102*(B1), 543-552. doi: 10.1029/96JB02933

Smith, E. C., Baird, A. F., Kendall, J. M., Martin, C., Brisbourne, A. M., & Smith, A. M. (2017). Ice fabric in an Antarctic ice stream interpreted from seismic anisotropy. *Geophysical Research Letters*, *44*, 3710–3718. doi: 10.1002/2016GL072093

Thorsteinsson, T., Kipfstuhl, J., & Miller, H. (1997). Textures and fabrics in the GRIP ice core. *Journal of Geophysical Research*, *102*. doi: 10.1029/97JC00161

Ting, T. C. T. (1996). Anisotropic elasticity. In (p. 53–56). Oxford University Press.

Touzi, R., & Lopes, A. (1999). Coherence Estimation for SAR Imagery. *IEEE Transactions of Geoscience and Remote Sensing*, *37*(1), 135–149. doi: 10.1109/36.739146

van der Veen, C. J., & Whillans, I. M. (1994). Development of fabric in ice. *Cold Regions Science and Technology*, *22*, 171–195. doi: https://doi.org/10.1016/0165-232X(94)90027-2

Wang, Y., Thorsteinsson, T., Kipfstuhl, J., Miller, H., Dahl-Jensen, D., & Shoji, H. (2002). A vertical girdle fabric in the NorthGRIP deep ice core. *Journal of Glaciology*, *35*, 515–520. doi: https://doi.org/10.3189/172756402781817730

Woodcock, N. (1977). Specification of fabric shapes using an eigenvalue method. *Geological Society of America Bulletin*, *88*, 1231–1236.

Category	Symbol	Description
Ice motion	$\mathbf{D}$	3×3 strain-rate tensor
	$\bar{\boldsymbol{S}}$	3×3 deviatoric stress tensor
	θ_x	Azimuthal angle of ice flow in polarstereographic coordinates
	θ_{min}	Azimuthal angle of x_{min} (horizontal compression axis)
Fabric	$\mathbf{a}$	3×3 second order orientation tensor
	$G = 2(a_2 - a_1)$	Girdle strength parameter
	$P = (a_3 - a_2)$	Pole strength parameter
	θ_G	Azimuthal angle of x_2 axis (assumes x_3 vertical)
	θ_P	Azimuthal angle of x_3 axis (assumes x_1 vertical)
Rheology	$\boldsymbol{\psi}$	6×6 representation of 4th order fluidity tensor
	K	6×6 rotation matrix
	β, γ	Anisotropic viscosities in flow law
Radar analysis	S	2×2 scattering matrix
	c_{hhhv}	*hhvv* (polarimetric) coherence
	ϕ_{hhhv}	*hhvv* coherence phase (co-polarized phase difference)
	$\Delta\epsilon'$	Ice crystal birefringence
	$\bar{\epsilon}$	Mean (polarization averaged) permittivity
	H, V	Polarizations in quad-polarized (fixed) basis
	h, v	Polarizations in multi-polarized (rotating) basis
Coordinate systems	x_1, x_2, x_3	Principal axes (eigenvectors) of $\mathbf{a}$ and $\boldsymbol{\psi}$
	x, y, z	Local ice-flow coordinates (x along flow, y across flow)
	x_{min}, x_{max}	Horizontal principal axes of $\mathbf{D}$ (compression and extension)
	θ	Azimuthal bearing angle in polarstereographic coordinates

Table A1. Glossary of key symbols

Supporting Information for 'Radar characterization of ice crystal orientation fabric and anisotropic rheology within an Antarctic ice stream'

T. M. Jordan [1,2,3], C. Martin [4], A. M. Brisbourne [4], D. M. Schroeder [2,5], and A. M. Smith [4]

[1]School of Geographical Sciences, University of Bristol, Bristol, UK.

[2]Department of Geophysics, Stanford University, Stanford, USA.

[3]Plymouth Marine Laboratory, Plymouth, UK.

[4]British Antarctic Survey, Cambridge, UK.

[5]Department of Electrical Engineering, Stanford University, Stanford, USA.

Contents of this file

1. Supporting information for polarimetric data analysis methodology.
2. Polarimetric coherence analysis at all measurement sites.
3. Polarimetric coherence analysis for the full ice column.
4. Sensitivity of fabric estimates to different coherence window sizes.

1. Supporting information for polarimetric data analysis methodology.

Figure S1 shows a flow-diagram illustrating the key steps of the polarimetric coherence method. To take into account measurement uncertainty the data-fits are performed over a set of 50 ensemble members incorporating azimuthal error on the antenna alignment and coherence phase uncertainty. Steps 2,3 and 5 run over each ensemble member.

In Step 2 we account for alignment uncertainty assuming $\sigma_\theta = \pm\ 5^\circ$ which is modeled as a Gaussian random variable for each measured HV mode combination. We account for coherence uncertainty in Step 3 by then perturbing each ϕ_{hhvv} pixel with the phase error, $\sigma_{\phi_{hhvv}}$ (see equation (3) in the main article), again modeled as a Gaussian random variable. The phase derivative, $\frac{\phi_{hhvv}}{dz}$, which is used directly in the fabric estimation, is then computed within Step 3 for each ensemble member with these two sources of uncertainty incorporated.

The data-fits in Step 5 are carried for each ensemble member using the azimuthal symmetry constraint for $\frac{\phi_{hhvv}}{dz}$ about $\theta = \theta_G$. This is illustrated visually in Figure 4 in the main article, using synthetic data and the backscatter model, Step 4. To computationally implement the constraint, and solve for $\theta_G(z)$ at each ice depth, we minimize a cost function in each range bin of the form

$$\theta_G = \arg\min_{\theta_n} \left\{ \sum_{\theta_n=0^\circ}^{\theta_n=180^\circ} \sum_{\theta_m=0^\circ}^{\theta_m=180^\circ} w_m \sqrt{\left(\frac{d\phi_{hhvv}}{dz}(\theta_n + \theta_m) - \frac{d\phi_{hhvv}}{dz}(\theta_n - \theta_m) \right)^2} \right\}, \qquad (1)$$

where w_m is a normalization weight and the indices n and m run over all of the azimuthal pixels (181 assuming an angular resolution of 1°). In the ideal case, when there is perfect reflection symmetry about θ_G, each $\left(\frac{d\phi_{hhvv}}{dz}(\theta_n + \theta_m) - \frac{d\phi_{hhvv}}{dz}(\theta_n - \theta_m) \right)$ term in the summation over θ_m is zero, and the minimization results in $\theta_n = \theta_G$ (or $\theta_n = \theta_G \pm 90^\circ$) at a

given ice depth. Once the profile $\theta_G(z)$ is obtained, $G(z)$ is obtained using equation (4) in the main article.

Steps 2-5 repeat over all ensemble members, and ensemble means and standard deviations evaluated at each ice depth give the mean and propagated uncertainty for $\theta_G(z)$ and $G(z)$.

2. Polarimetric coherence analysis at all measurement sites

Figures S2 and S3 show polarimetric coherence analysis for sites along Transect A that were not included in the main article. As in the main article, we assume a vertical girdle description of the fabric (corresponding horizontal pole parameters can be obtained from $\theta_P = \theta_G$ and $P = \frac{G}{2}$). The series of plots illustrates the relative counter-clockwise rotation of $\theta_G(z)$ in shallow ice as the measurements become closer to the shear margin. The increase in G in shallower ice toward the shear margin is also evident from the faster phase cycles.

Figures S4 and S5 show polarimetric coherence analysis for additional sites along Transect B. Sites B3-B5, Figure S5, are all qualitatively similar to site B2 shown in the main article. Site B7 has a negligible phase gradient in shallower ice, Figure S5b. This is likely to correspond to a near-random fabric (as the vertical fabric eigenvalue is likely to be relatively low in shallower ice). Sites B8 and B9, Figure S5b and c, show a qualitatively similar azimuthal rotation for $\theta_G(z)$ within the ice column ($\approx 90°$ at z $\approx$ 100 m) to site B10 in the main article.

3. Polarimetric coherence analysis for the full ice column

Figure S6 shows polarimetric coherence analysis for the full ice column at sites A1 and A6. In general, the coherence magnitude is not sufficiently high to make accurate fabric estimates throughout the ice column (based on the filtering step which requires $|c_{hhvv}(\theta_G, z)| > 0.5$). In deeper ice ($z > 1400$ m), however, there is a unit of high coherence magnitude where fabric estimates can be made. In this unit the vertical phase gradient is negligible, which results in locally fluctuating estimates for θ_G and negligible estimates for G. The estimates in this unit therefore support the existence of a tendency toward a vertically-orientated single maximum fabric (as the vertical fabric eigenvalue is likely to be high in deeper ice).

4. Sensitivity of fabric estimates to different coherence window sizes

Figure S7 shows the sensitivity of fabric estimates along Transect A for three different window sizes, W. An example of the coherence analysis for one of the sites (A6) is shown in Figure S8. The θ_G estimates are highly robust to the window size, and fall within the estimated uncertainty bounds, Figure S7a. The G estimates have a systematic decrease with window size, Figure S7b, although all window sizes capture the important trend of strengthening toward the shear-margin (sites A5-A9). The choice of W=40 m in the main article is thought to represent a good trade-off between desired vertical resolution and including enough range-cells to produce a robust coherence estimate.

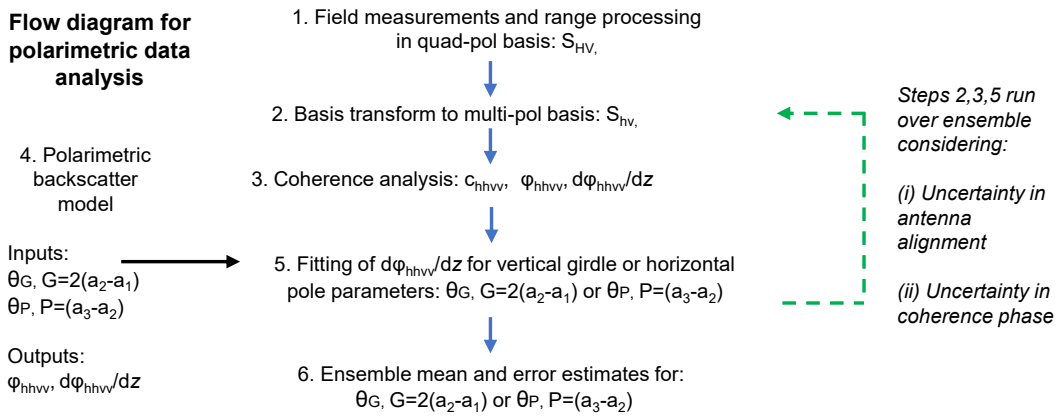

Figure S1. Flow diagram for polarimetric data analysis.

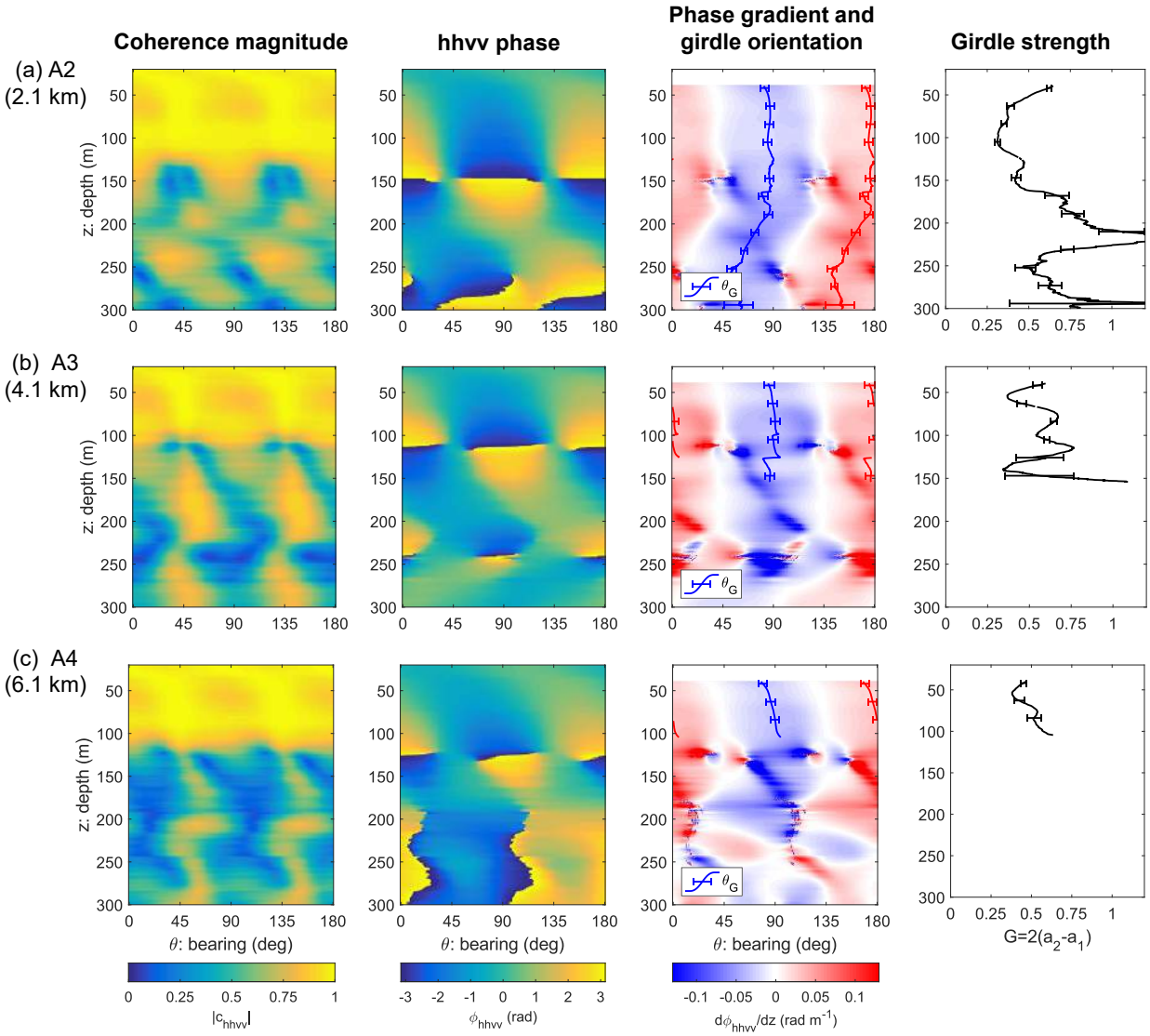

Figure S2. Polarimetric coherence analysis at sites: (a) A2, (b) A3, (c) A4. The depth-profiles for the girdle fabric estimates, $\theta_G(z)$ and $G(z)$ are shown in the center right and far right columns. A filtering step is applied such that fabric estimates require $|c_{hhvv}(\theta_G, z)| > 0.5$.

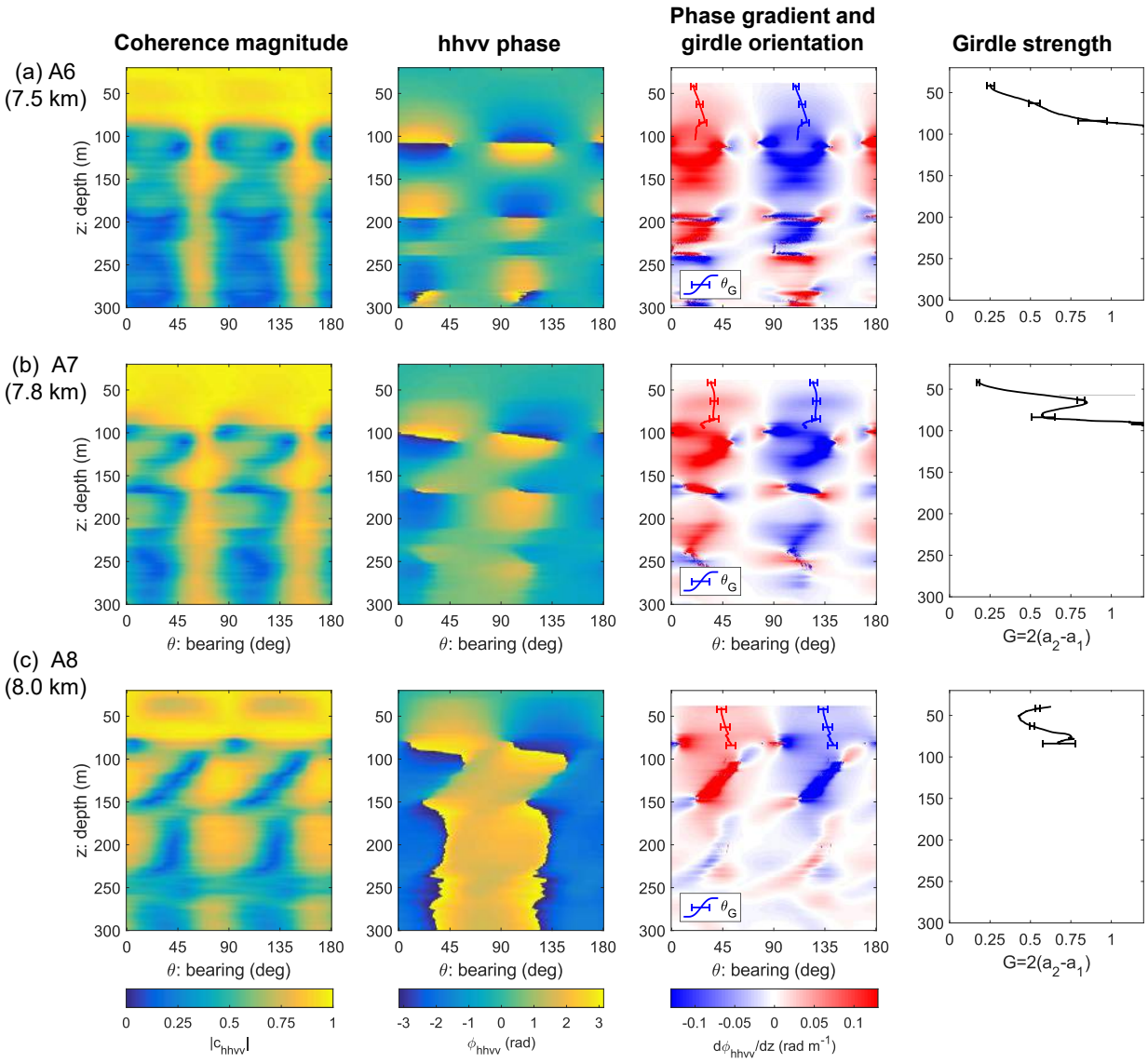

Figure S3. Polarimetric coherence analysis at sites: (a) A6, (b) A7, (c) A8.

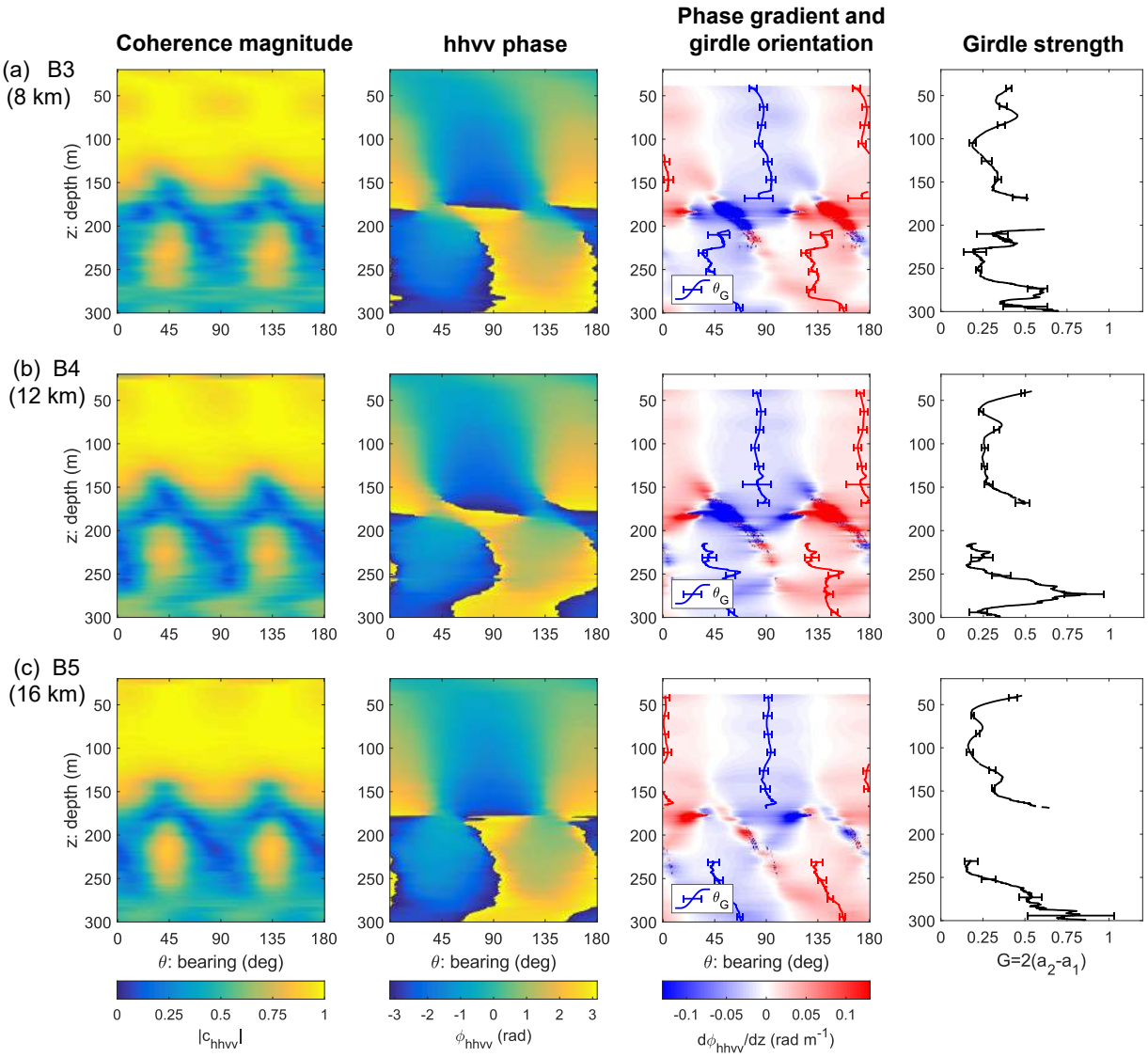

Figure S4. Polarimetric coherence analysis at sites: (a) B3, (b) B4, (c) B5.

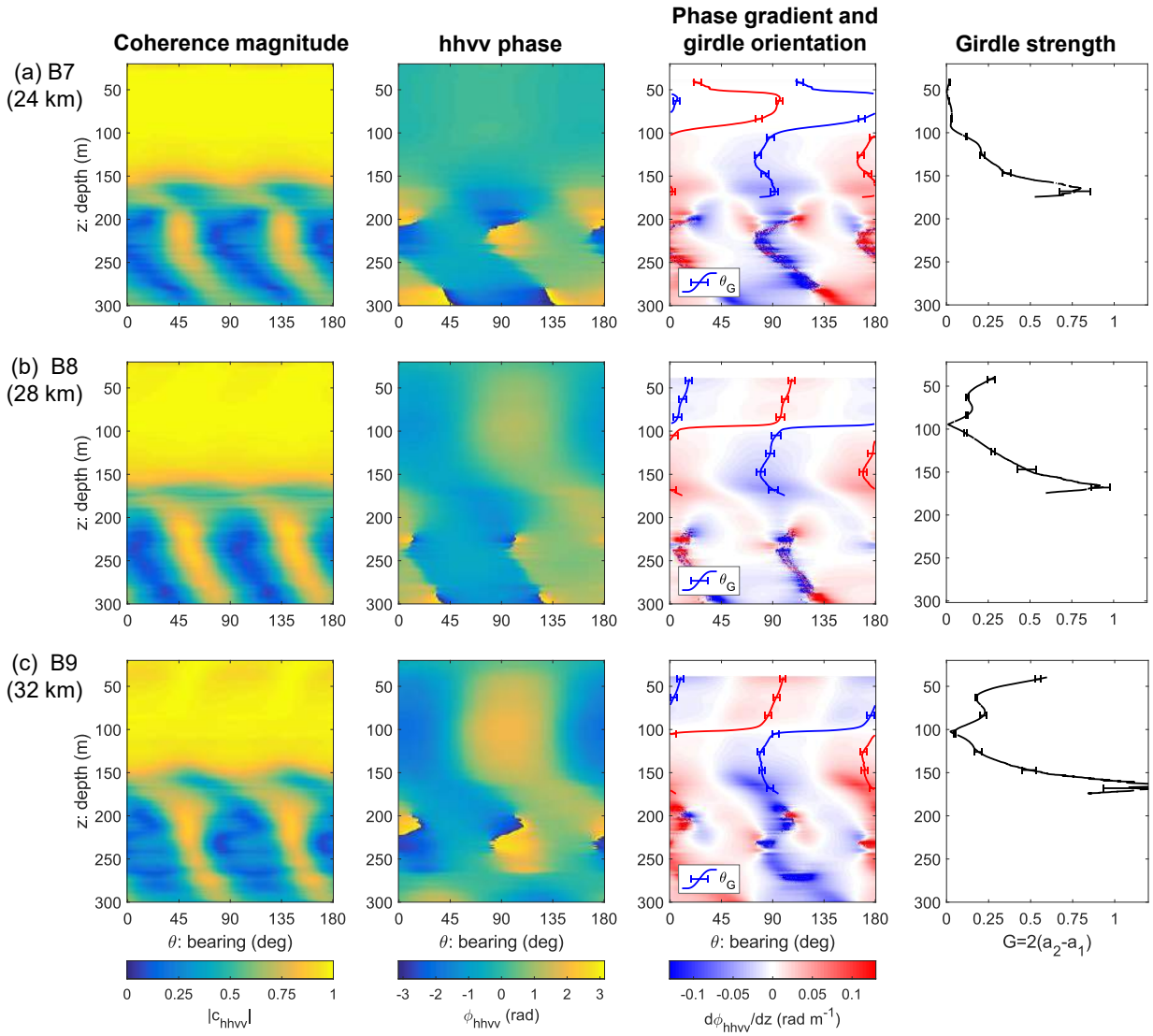

Figure S5. Polarimetric coherence analysis at sites: (a) B7, (b) B8, (c) B9.

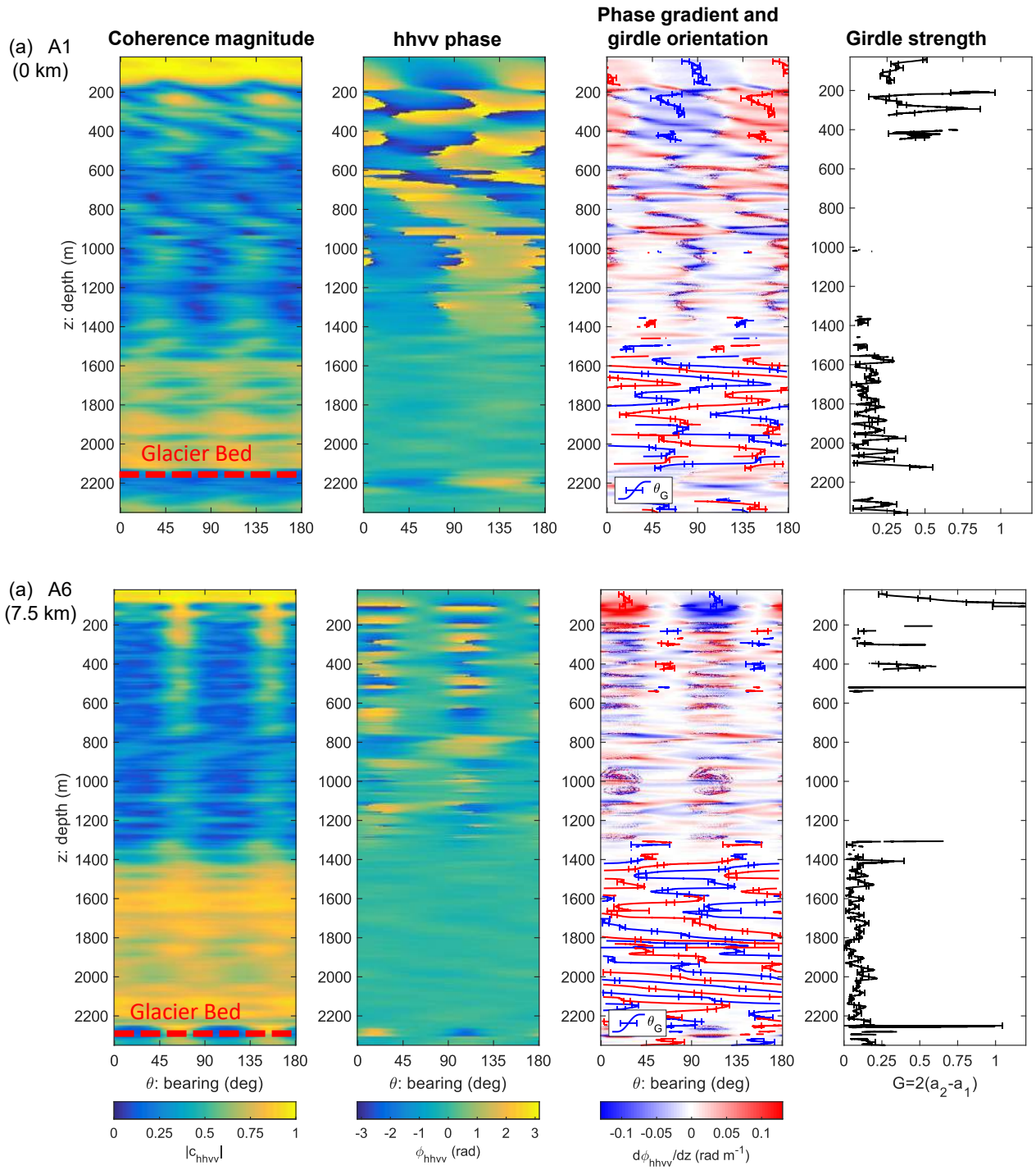

Figure S6. Full ice column polarimetric coherence analysis at sites: (a) A1, (b) A6.

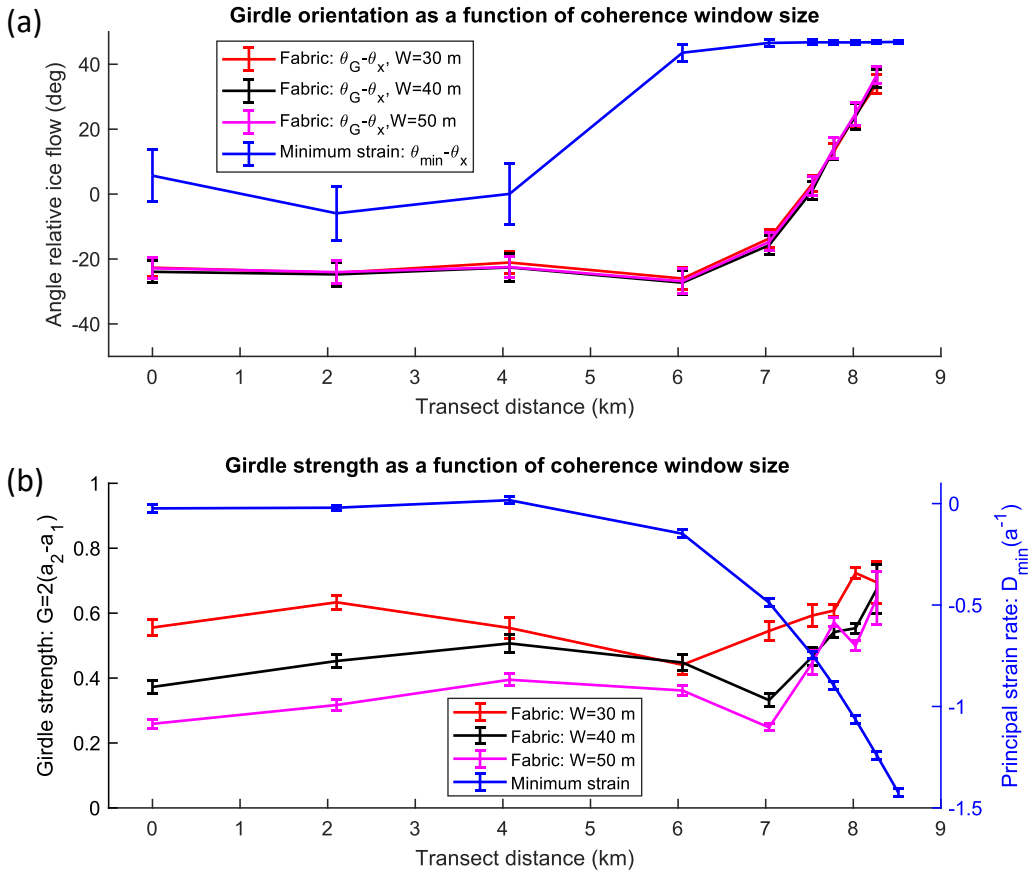

Figure S7. Sensitivity of fabric estimates for three different different window sizes, W (Transect A). (a) Girdle orientation in relation to ice flow, $(\theta_G - \theta_x)$. (b) Girdle Strength, G.

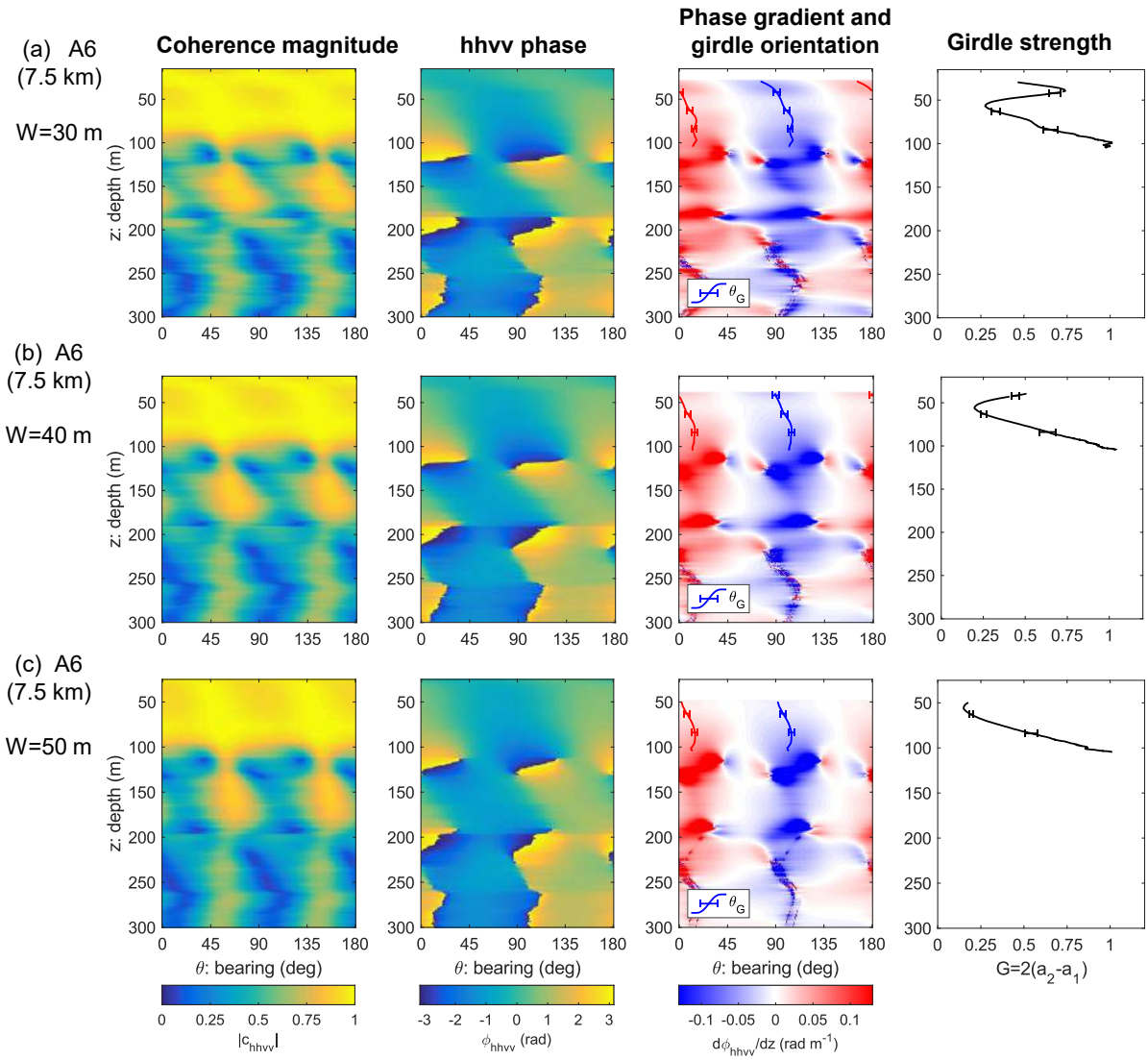

Figure S8. Polarimetric coherence analysis at site A6 for three different window sizes, W. (a) W=30 m. (b) W=40 m. (c) W=50 m.